Montanuniversität Leoben

Development and characterization of a new near-α-titanium alloy for high performance applications

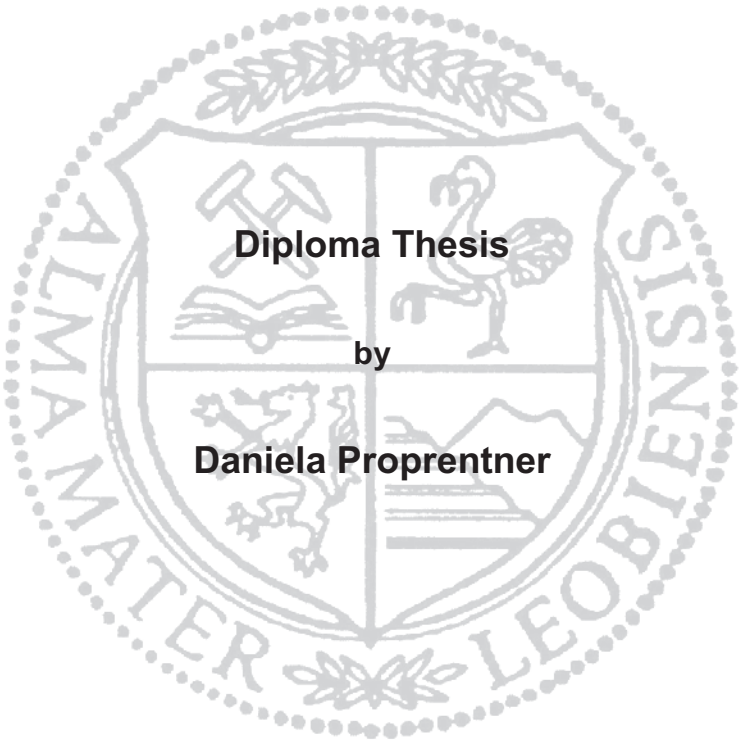

Diploma Thesis

by

Daniela Proprentner

Accomplished at the Department of Physical Metallurgy and Materials Testing at the University of Leoben in cooperation with the DaimlerChrysler AG.

Leoben, June 2007

Acknowledgement

An dieser Stelle möchte ich mich in erster Linie bei Herrn Prof. Dr. Helmut Clemens für die Themenstellung und fachliche Unterstützung bedanken.

Mein besonderer Dank gilt auch der ausgezeichneten Betreuung von Herrn Dr. Harald Chladil, der durch seine tatkräftige Unterstützung bei zahlreichen Versuchen und Diskussionen wesentlich zum Entstehen und erfolgreichen Abschließen dieser Arbeit beitrug.

Bedanken möchte ich mich auch für die exzellente Firmenbetreuung bei Herrn Dr. Rainer Joos, der mich sowohl bei meinem mehrmonatigen Aufenthalt in Stuttgart als auch nach meiner Rückkehr an die Montanuniversität hervorragend unterstützte.

Dank aussprechen möchte ich auch Frau Christine Möck, die mir ebenfalls in Stuttgart hilfreich zur Seite stand.

Ich danke allen Mitarbeitern und Mitarbeiterinnen des Departments Metallkunde und Werkstoffprüfung, die mir in der Zeit der Erarbeitung meiner Diplomarbeit immer mit Rat und Tat zur Seite standen.

Mein persönlicher Dank gilt meinen Eltern, meiner Schwester und meinen Freunden, die immer eine große und motivierende Stütze waren.

Ich widme diese Diplomarbeit meinen Eltern Irmgard und Thomas Proprentner und meiner Schwester Andrea Besold.

Contents

List of Symbols

AC	Air cooled
bcc	Body centered cubic
BSE	Back scattered electrons
E	Young's modulus
EBSD	Electron back scattered diffractometry
EDS	Energy dispersive X-ray spectroscopy
hcp	Hexagonal closed packed
HT	Heat treatment
IMI	Imperial Metal Industries
IS	Initial state
LCF	Low cycle fatigue
LCS	Large cross section
m.%	Mass percent
PQM	Pattern quality map
R_m	Tensile strength
R_p	Yield strength
SE	Secondary electrons
SEM	Scanning electron microscope
TEM	Transmission electron microscope
Timetal	Titanium metals corporation of America
T_α	α-transus temperature
T_β	β-transus temperature
VAR	Vacuum Arc Remelting
VBS	Valve blanks forging route S
VBT	Valve blanks forging route T
VBU	Valve blanks forging route U
WDS	Wave length dispersive spectroscopy
WQ	Water quenched
XRD	X-ray diffractometry
ε	Elongation
$\dot{\varepsilon}$	Deformation rate
σ_{UTS}	Ultimate tensile strength

1. Introduction

The original need of the aircraft industry for an efficient high temperature material drove the evolution of near-α-alloys, which started about 50 years ago [1]. By now, IMI 834 and Ti-1100 are the most important and advanced alloys up to a maximum working temperature of about 600℃. Because of their specific chemical composition, based on titanium and a combination of α- and β-stabilizers, one can adapt their microstructure to numerous patterns. Depending on the processing route lamellar or equiaxed microstructures can be achieved, and good creep resistance and high fatigue strength at elevated temperatures are the advantageous features. These are especially required for aircraft turbines, but can also be used for high performance automotive engines [2].

The new near-α-alloy NB4, which this diploma thesis will present, was developed and characterized to meet the material requisition of exhaust valves in competitive high performance engines. These valves have to withstand circa 800℃ for 8 to 10 hours and were originally made of γ-TiAl based alloys. Due to a change in competition rules - prohibiting an intermetallic content of the alloy over 50 vol.% - the material switched to the already known near-α-alloy IMI 834. The competitive need of further improvement of the exhaust valves performance led to the development of the new near-α-alloy NB4. This alloy was designed based on thermo-dynamic calculations in the run-up to this thesis by the Department of Physical Metallurgy and Materials Testing at the University of Leoben in cooperation with DaimlerChrysler AG. Based on the knowledge of other near-α-alloys, such as IMI 834 or Ti-1100, the alloying elements were selected. The motive was to design NB4 with an intermetallic α_2-content that should strengthen the matrix, close to the 50 vol.% border. The weakening β-phase was tried to suppress.

The valves are produced in a two-step procedure. First, a rod is extruded and in the second step a valve blank is formed by a combination of extruding and forging.

Main focus of this thesis was laid upon the development of heat-treatments to adjust a microstructure that offers the best mechanical properties, especially in terms of tensile strength at elevated temperatures. Studies of the microstructure of the as-extruded and annealed state combined with hardness tests and tensile tests led stepwise to an optimal heat-treatment procedure. Annealing has been accomplished at temperatures between 650 and 850℃ for 2 up to 24 hours and annealing around T_β. For a better understanding the evolution of the microstructure during deformation,

tests in a dilatometer were conducted in order to simulate the forging step. Phase analysis was performed by means of quantitative microstructure analysis as well as by Rietveld analysis of XRD data. EBSD and TEM were applied to characterize and quantify the microstructure. The microstructure at transition between the stem and the head was of high importance since this part of the valve is exposed to the highest temperature and strength.

Another point of concern due to the high temperature exposure of the component was the resistance against oxidation. Therefore, the influence of niobium was investigated and a comparison with other near-α-alloys was made. The valve sections with severe exposure to oxidation are the lower surface of the head, but also the remaining part of the head and partly the stem.

The thesis will start of in the following chapter with an overview about alloying concepts of Ti-alloys and near-α-alloys. The third chapter describes the methods used for characterization. Chapter 4 will present results and the discussion, and is followed by a final summary.

2. Theoretical principles

2.1. Titanium alloys

The properties of titanium alloys meet the standards of various applications in a wide range of fields, e.g. aerospace, automotive, sports or medical industry. Especially the first two applications do require microstructural stability at high temperatures. Conventional titanium alloys can be used up to about 600℃, whereas TiAl-based alloys yet achieve a competitive specific strength at 600 - 800℃ [2, 3]. Fig. 2-1 compares different titanium alloys and γ-TiAl-based alloys with other structural materials in reference to their specific strength at different temperatures.

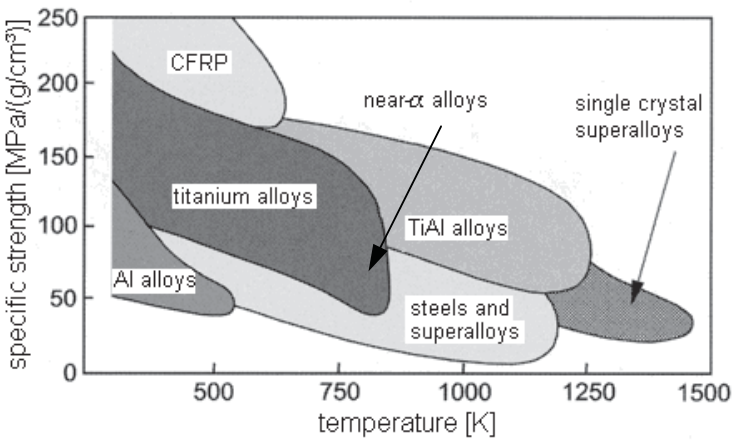

Fig. 2-1: Comparison of Ti-alloys, γ-TiAl based alloys and other conventional structural materials such as Al-alloys and CFRP (carbon fiber reinforced polymers) regarding the specific strength at elevated temperatures [2].

The high temperature application of titanium alloys is basically limited by the loss in strength, whereas the oxidation resistance plays a decisive role as well.
Fig. 2-2 shows the phase diagram of the two alloy components titanium and aluminum and the appearing crystal structures. At low Al contents and below the α- and β-transformation temperature (T_α, T_β) α-Ti, a hexagonal closed packed (hcp) structure is present. Al contents between 25 and 35 m.% promote the formation of the ordered hcp α_2-Ti_3Al structure. Aluminum atoms are substitutional integrated into the lattice as shown in the unit cell of Fig. 2-2. Further increase of the Al content

forms the face centered tetragonal γ-TiAl phase. The transformation temperature T_β of pure titanium is at 882℃ and displays the borde r to the high temperature β-Ti phase, which has a body centered cubic (bcc) structure. The α-Ti and the β-Ti phase fields are separated by a two phase α-β-field and indicated by the phase transformation temperatures T_α and T_β. Both temperatures increase with an higher Al content as shown in Fig. 2-2 [2].

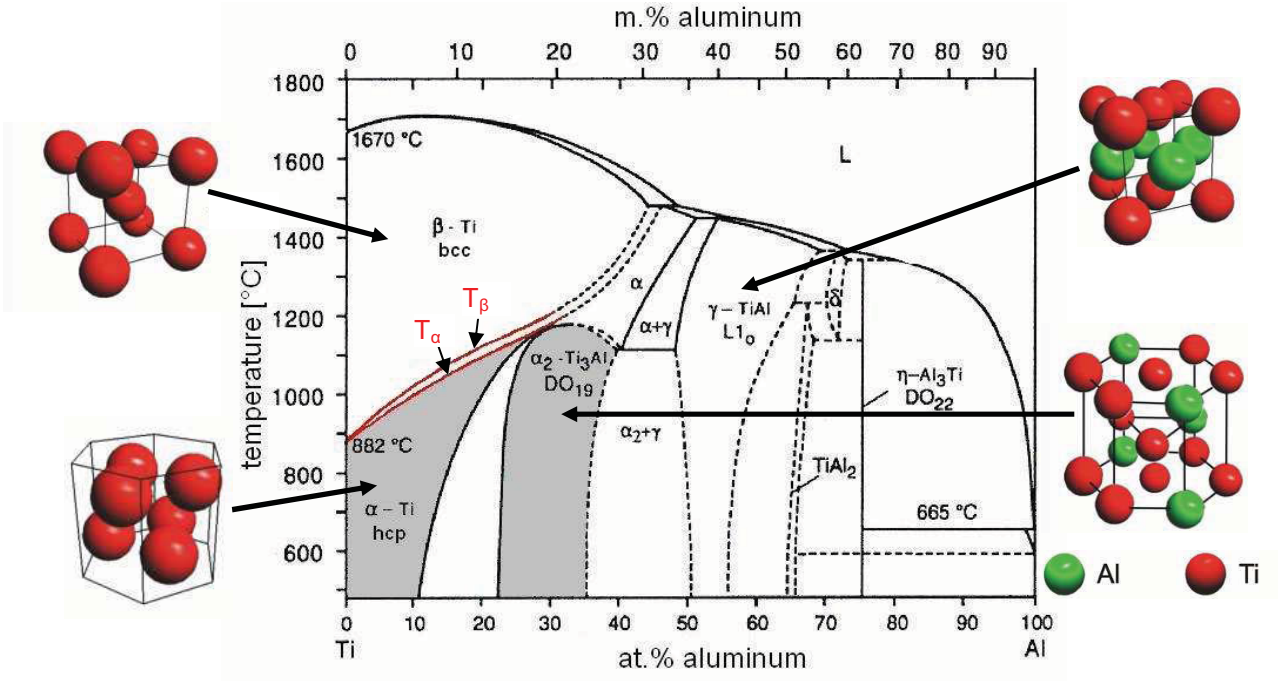

Fig. 2-2: Titanium – aluminum phase diagram with the crystal structures of the constituting phases α-Ti, β-Ti, α_2-Ti_3Al and γ-TiAl [2].

By cooling from the β-Ti phase region into the α-Ti phase region, the lattice can either undergo a martensitic transformation or a transformation based on diffusion depending on cooling rate and alloy composition. The relationship of Burgers [4], correlating corresponding planes and directions in the α- and β-lattice, can be applied for both. Therefore, the $(110)_\beta$ plane and the $[1\text{-}11]_\beta$ direction in the bcc lattice correspond to the according $(0002)_\alpha$ and $[11\text{-}20]_\alpha$ in the hexagonal lattice. Fig. 2-3 demonstrates this transformation and indicates the involved planes.

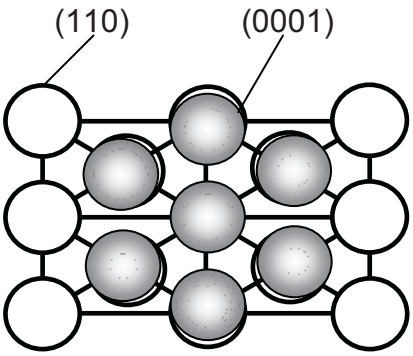

Fig. 2-3: Transformation of bcc β-Ti to the hcp α-Ti according to the Burgers relationship [2].

High cooling rates promote martensitic transformation. Within this transformation, a plate shaped volume changes from the bcc structure of β-Ti to the hcp structure of α-Ti by sheering. The resulting martensite may form two different types. Massive or packed martensite is significant for pure Ti or barely alloyed alloys as well as for alloys with low martensitic transformation temperatures. An unstructured microstructure that contains packets of small parallel α-plates, is typical for massive martensite. α-plates, with a thickness of 0.5–1 µm, are usually not visible with an optical light microscope. The second type is called acicular martensite. It is also composed of α-plates although not showing the ordered parallelism of the massive martensite. Due to the high cooling rate, the formed α'-martensite is supersaturated with β-stabilizing alloying elements (i.e. Mo, Nb, V). A high content of elements in solubility results in a third martensitic type, the so-called α''-martensite. As a result of the increasing number of dissolved atoms the hexagonal lattice distorts and changes to an orthorhombic unit cell [5].

Low cooling rates enable a transformation based on nucleation and diffusion. Upon reaching the α-β-phase field, α-Ti starts to form a continuous grain boundary layer around the original β-grains. Nucleating at the original β-grain boundaries or at the newly formed α-layer, α-plates grow into the original β-grain. This takes place on all sides of the former β-grain until the plates meet and hinder each other in the middle of the former β-grain. Groups of plates, emerging close to each other, grow parallel and belong to the same Burgers relationship. The resulting lamellar microstructure consists of α-plates in a retained β-matrix, often incorrectly called β-plates [5]. This development is shown in Fig. 2-4.

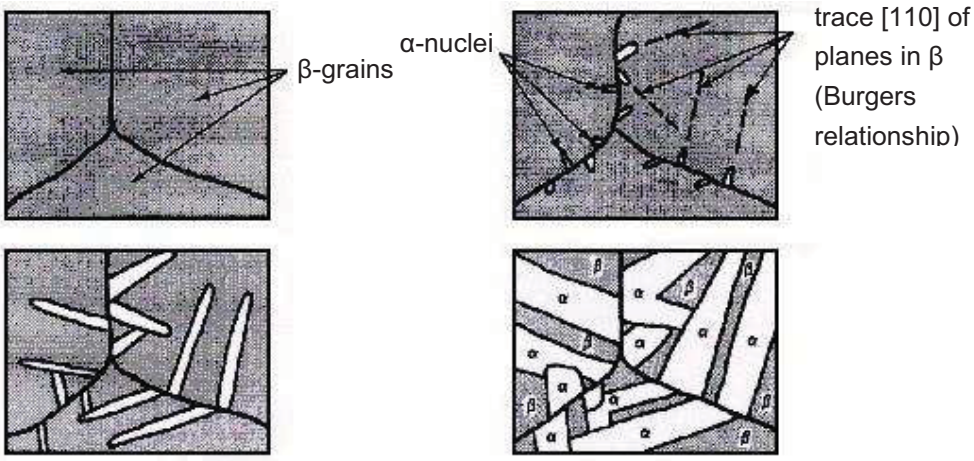

Fig. 2-4: Development of α-plates through nucleation and diffusion according the Burgers relationship [6].

2.2. Classification of titanium alloys and influence of alloying elements

The classification of titanium alloys corresponds to the present alloying elements, which dominate their properties. An overview of the effects of alloying elements is given in Fig. 2-5. They can either be α-stabilizing, β-stabilizing or neutral and their presence divides titanium alloys accordingly into α-, β- and intermediate alloys (see Fig. 2-5). Thanks to their excellent oxidation behavior, deformability and high specific strength α-alloys are primarily used in the chemical and process engineering industry. Near-α-alloys and their combination of excellent creep behavior and high strength are used for high temperature applications up to 600℃. α-β-alloys are highly popular in aerospace industry. On the one hand they can be used because of the balanced properties of high strength and toughness, on the other hand for applications in gas turbines at elevated temperatures up to 400℃. Finally, metastable β-alloys were developed to optimize high strength and toughness, though a restriction is given by the high specific weight, modest weldability, poor oxidation and a complex microstructure [2,5,8].

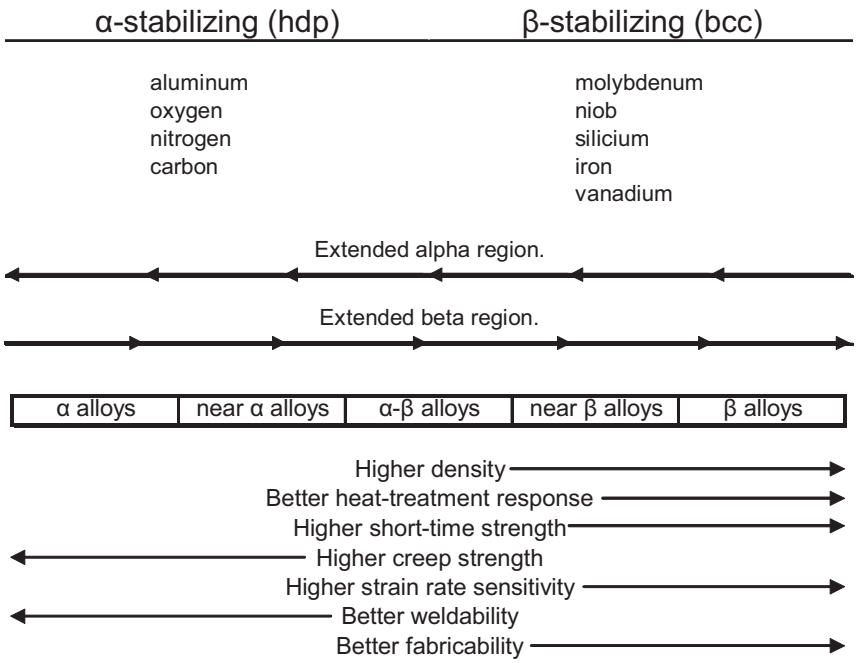

Fig. 2-5: Classification of titanium alloys into classes, depending on components. Different classes promote different properties [9].

Aluminum and interstitial alloying elements such as O, C and N stabilize the α-Ti phase and augment the α- as well as the β-transus temperature (see Fig. 2-6). As the major α-stabilizer, Al improves the mechanical properties (tensile strength R_m, creep strength and Young's modulus E). By increasing the O content, the α_2-Ti_3Al phase is stabilized against the α-Ti phase. However, increasing the intermetallic α_2-phase fraction improves the tensile strength and the Young's modulus, though it decreases the oxidation behavior and increases embrittlement [2]. To find an adequate balance, the Al-content is limited by the Al-equivalent, further stated in chapter 2.3.

Tin, as an α-stabilizer, increases strength without the drawback of embrittlement as known for Al, though the stabilizing effect of Sn is weaker than that of Al [5].

Carbon improves strength as well as fatigue properties. Additions of C increase the α-β-phase region in temperature and expands the phase field because of the formation of carbide precipitates [10]. Consequently, T_α moves to higher temperatures, whereas T_β is shifted to lower ones [10].

Mo, Nb, Ta, V, Fe, Mn, Cr, Co, Ni, Cu, Si, and H are β-Ti stabilizing elements, which result in a decrease of the transition temperatures T_α and $T_{\beta,}$ as shown in Fig. 2-6. There are two different kinds of β-stabilizers, namely β-isomorphous and β-eutectic elements. Isomorphous elements, such as Mo, Nb, Ta and V, are completely miscible in the β-phase and promote solid solution strengthening of the β-phase. Eutectoid forming elements, e.g. Fe, Mn, Cr, Co, Ni, Cu Si, and H promote the formation of intermetallic compounds [2,8].

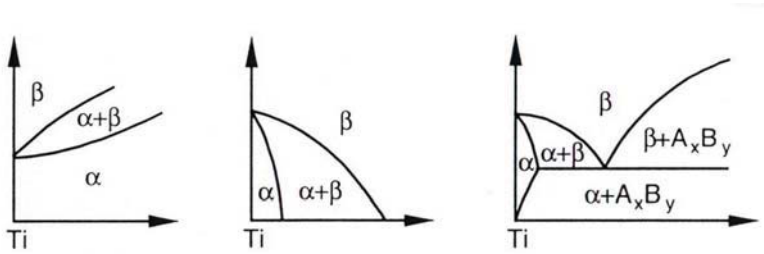

α-stabilizing β-stabilizing

β-isomorphous β-eutectic

(Al, O, N,C) (Mo, V, Ta, Nb) (Fe, Mn, Cr, Co, Ni, Cu, Si, H)

Fig. 2-6: Influence of α- and β-stabilizing elements on the phase diagram of Ti-alloys [2].

The alloying element Si is used to improve creep properties and will be described in more detail in the following chapter.

2.3. Near-α-alloys

In near-α-alloys, both α- and β-stabilizing alloying elements such as Al, O, Mo, Nb, and Si are used. Therefore, α-Ti, α_2-Ti_3Al and, at higher temperatures, residual β-Ti are the present phases. Generally, the Al content is limited to about 9 m.%. A higher content results in the formation of the α_2-Ti_3Al phase, which is further specified by the Al equivalent [11]:

Al eq. = m.% Al + 1/3 m.% Sn + 1/6 m.% Zr + 10 m.% O < 9 m.%.

The first commercially used near-α-alloy was Ti-811, released in 1960 by the Titanium metals corporation of America (Timetal) [2]. Alternately, Timetal and the English Imperial Metal Industries (IMI) released alloys reaching higher service temperatures. This trend in the development of near-α-alloys is illustrated in Fig. 2-7

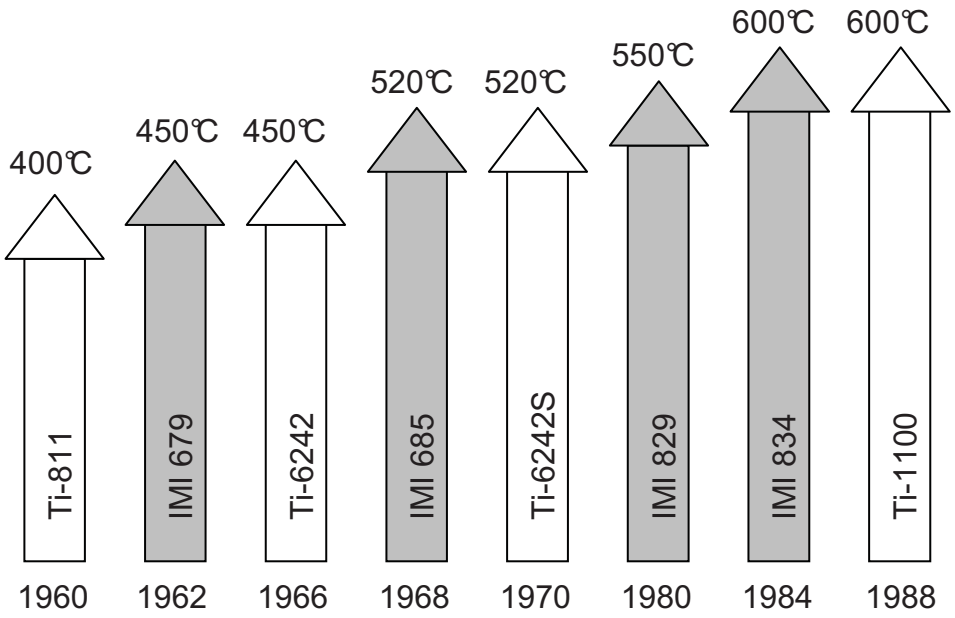

Fig. 2-7: Chronological development of important near-α-alloys and their maximum application temperatures [12].

The far most important and latest released alloys are IMI 834 and Ti-1100 – the chemical composition is shown in Tab. 2-1. Both are in use for aircraft turbines and are designed for service temperatures up to 600℃.

Tab. 2-1: Chemical composition of the near-α-alloys Ti-811, IMI 834 and Ti-1100 and Ti-6242(S) in m.% [2,13,14].

	Ti	Al	Sn	Zr	Mo	Nb	Si	V	C
Ti-811	bal.	8	---	---	1	---	---	1	---
IMI 834	bal.	5.8	4	3.5	0.5	0.7	0.35	---	0.06
Ti-1100	bal.	6	2.7	4	0.4	---	0.4	---	---
Ti-6242	bal.	6	2	4	2	---	---	---	---
Ti-6242S	bal.	6	2	4	2	---	0.1	---	---

2.3.1. The influence of the alloying element Silicon

Despite the small alloying content, Si plays an as much as important role as Al in developing near-α-titanium alloys for high temperature applications. This was first discovered by Seagle et. al. [15] in the 1970s and commercially introduced by the addition of 0.1 m.% silicon to the alloy Ti-6242, becoming Ti-6242S (see Tab. 3-1 for chemical compositions). Fig. 2-8 displays the effect of the Si content on the alloy IMI 834. A content of about 0.5 m.% is used in commercial near-α-alloys to increase high

temperature strength and creep resistance by precipitation of silicides of the type Ti_5Si_3 and $(Ti,Zr)_5Si_3$ [16].

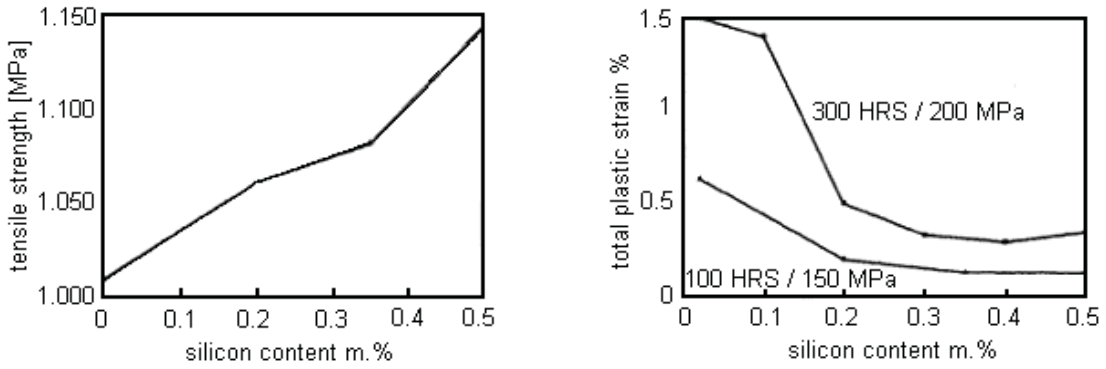

a) b)

Fig. 2-8: Influence of Si content on a) tensile strength and b) total plastic strain of near-α-alloy IMI 834 [16].

The hardening effect is based on Si in solid solution as well as in form of silicide precipitates. The solubility of Si in the α-Ti phase is limited to 0.47 m.% and it becomes less as temperature decreases. Additional β-stabilizers increase the Si-solubility limit. Another impact is given by ageing and stabilizing heat-treatments. Annealing above the silicide solution temperature is required to retain the silicon in solid-solution state. Above service temperatures of 450℃, silicides start precipitating heterogeneously on dislocations or the decomposition of β-Ti into α-Ti and silicides starts. Depending on their history of origin, the precipitates size range between 0.01 µm and 5 µm [16].

2.3.2. Examples of conventional near-α-alloys

IMI 834 released by the English Imperial Metal Industries (IMI) and the Ti-1100 promoted by the Titanium metals corporation of America (Timetal) were both developed for a working temperature of 600℃ - the highest so far [12]. In the following two chapters, the main properties of these alloys will be discussed in more detail.

2.3.2.1. IMI 834

This alloy was primarily developed for the application in compressor discs and blades of gas turbines, working at maximum temperatures of about 600℃. Adequate forging routes and heat-treatments followed by appropriate cooling proceedings provide a

wide variety of different microstructures [9,17]. As-received material from IMI demands a sequence of solution annealing in the α-β-phase field, followed by air cooling. After an ageing treatment at 600℃ and sub sequently air cooling, a microstructure with the best mechanical properties, such as fracture toughness, low cycle fatigue and creep strength, can be achieved. This sequence of solution treating, air cooling and annealing is shortly called ST-AC-A. After solution annealing, primary α-Ti is embedded in an acicular β-matrix. Heat-treatments below T_β increase the volume fraction of α-Ti, whereas annealing above T_β provides an acicular microstructure of β-grains. The grain size expands, as the annealing temperature is raised [9]. The aging treatment results in a microstructure of 7.5-10 vol.% of primary α-Ti particles in a matrix of acicular transformed β-Ti [18], a so-called duplex structure [19]. It shows the best performance of creep strength, low cycle fatigue properties and resistance against crack propagation. Investigations done by transmission electron microscopy (TEM) unveiled platelets of α_2 and β between α-platelets and precipitates of silicides, characterized to be $(TiZr)_5Si_3$ [17].
The evolution of microstructure throughout thermo-mechanical processing was investigated by numerous studies [18,20,21,22]. During deformation, dynamic recovery and recrystallization play a key role. After discharging the load, grain growth, static recovery and recrystallization are the prevailing mechanisms [21]. Processing, for example forging can generally be done in the α-β-region or above T_β. The α-β-route results in a fine equiaxed microstructure, whereas, lower annealing temperatures decrease the grain size (Fig. 2-9 a and b) which improves the low cycle fatigue (LCF) behavior. In contrast to that, the β-forging route leads to an acicular microstructure (Fig. 2-9 c) and, therefore, enhances the creep strength and fracture toughness [9].

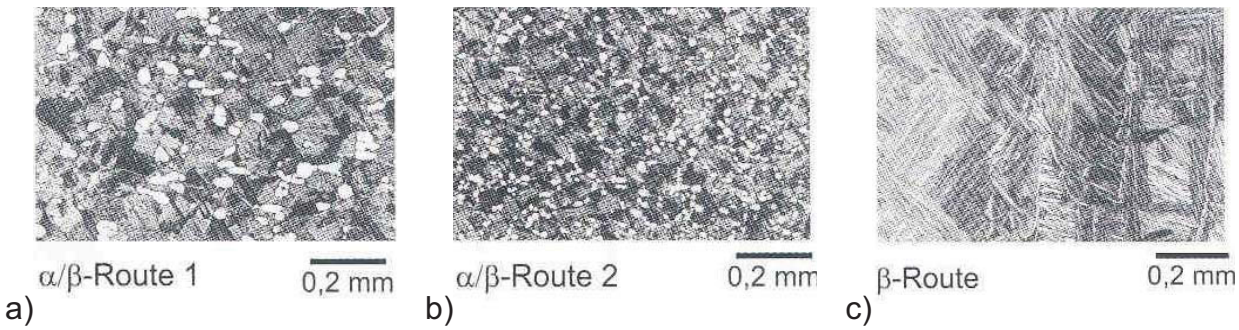

Fig. 2-9: Microstructures of IMI 834 after α-β-forging at a) high and b) low temperatures and c) β-forging [9].

Wanjara et al. [21] simulated a 2-step deformation process starting with an ingot. In the first step, a wrought product is formed by β-forging. A second closed-die forging step produces the final shape by α-β-forging. Typical flow curves are displayed in Fig.

2-10, showing the influence of forging temperature and strain rate. Forging in the β-single phase region (T_β~1000℃) shows an early stress peak rising to the t rue yield stress point, followed by a continuous flow softening. The α-β-route exhibits a definite peak and is again followed by flow softening. Distinctive for the α-β-route is a steady-state regime of flow stresses at higher strains compared to the β-forging route. Both routes were accompanied by flow softening, but only supertransus forging of IMI 834 showed strain hardening, attributed to high strain rates and minor flow softening.

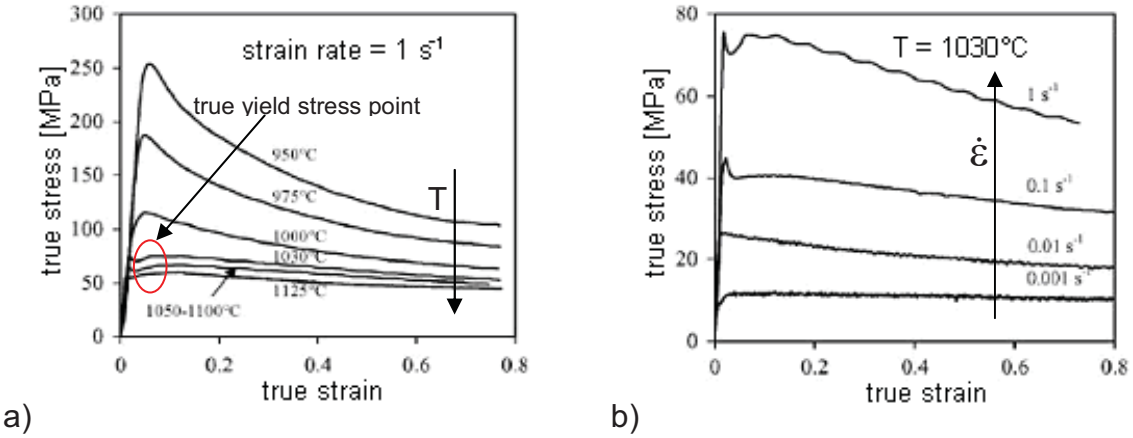

Fig. 2-10: Effect of a) forging temperature and b) strain rate on the flow behavior of IMI 834 [21].

Since β-forging is important for this diploma thesis, a closer look on the microstructure must be taken. Fig. 2-11 presents microstructures after different deformation tests above T_β with a variation of the strain rate. In fact all microstructures are composed of original (deformed) β-grains (1) and recrystallized β-grains (2).

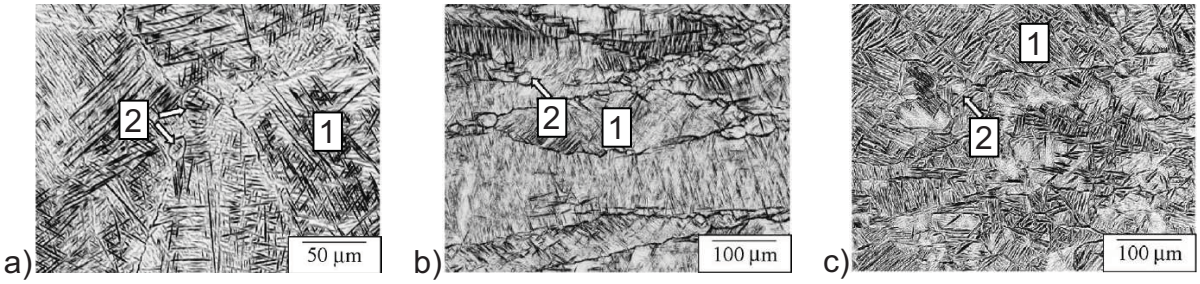

Fig. 2-11: Microstructures of IMI 834 , deformed above T_β (1050℃) a) strain rate and true strain of a) 1 s^{-1} and 0.2, b) 1 s^{-1} and 0.8 and c) 0.01 s^{-1} and 0.8. (1) indicates original β-grains and (2) recrystallized β-grains [20].

The comparison of tensile properties (σ_y, σ_{UTS}) determined at room temperature on the one hand and 600℃ on the other hand demonstrated a significant effect of temperature, as shown in Tab. 2-2. An increase of ductility and various ductility parameters, such as uniform elongation ε_u, total elongation ε_t and reduction in area RA, could be achieved with elevated temperature.

Tab. 2-2: Tensile properties of the alloy IMI 834 in the (α-β) ST-AC-A condition derived at room temperature and 600℃ [17].

T	σ_y [MPa]	σ_{UTS} [MPa]	σ_{UTS} / σ_y	ε_u (%)	ε_t (%)	RA (%)
RT	945	1012	1.07	7.9	14.5	14.1
600℃	528	628	1.19	11.5	26.3	45

2.3.2.2. Ti-1100

While IMI 834 was primary designed for optimum high-temperature low-cycle fatigue behavior, Ti-1100 was designed for high temperature creep resistance. The main difference is the proposed optimum microstructure of Ti-1100. Timet recommends forging above T_β followed by air cooling to achieve a completely lamellar structure, consisting of large transformed β-grains. This microstructure shows strong advantages for creep resistance and also promotes good fatigue crack growth properties when compared to fine grained microstructure of IMI 834 [23].
Results of thermo-mechanical treated samples are shown in Fig. 2-9. The light optical image of Fig. 2-9 displays Ti-1100, when thermo-mechanically treated slightly above T_β and high in the β-region. A comparison indicates a strong increase of the volume fraction of β-grains as well as a coarsening of the laths with higher temperatures [18].

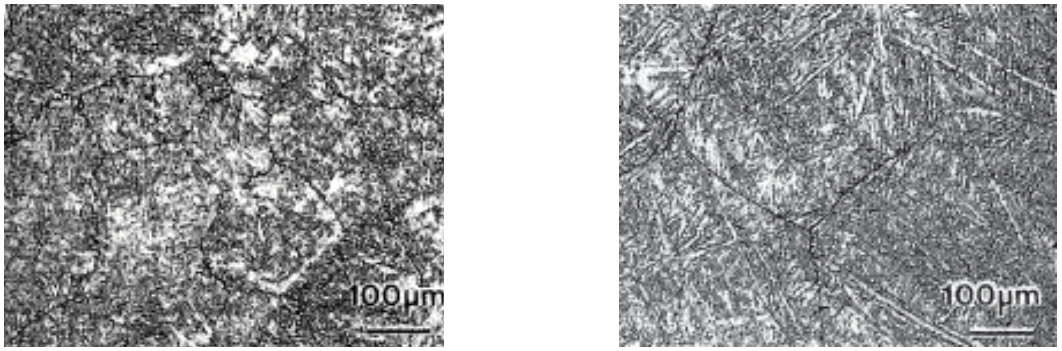

Fig. 2-12: Ti-1100, which was heat-treated above T_β: a) 1020℃ and b)1060℃. Higher temperature results in the appearance of larger grains [18].

The effects of the heat-treatment respectively the thermo-mechanical treatment on mechanical properties can be shown in terms of tensile properties at room temperature and elevated temperatures. By raising the tensile test temperature, strength decreases and elongation increases. These tendencies are enforced at higher temperatures. The influence of static heat-treatments below and above T_β on the tensile properties of Ti-1100 is displayed in Figs. 2-13 a) and b). Effects of thermo-mechanical treatments are shown in Figs. 2-13 c) and d) [18].

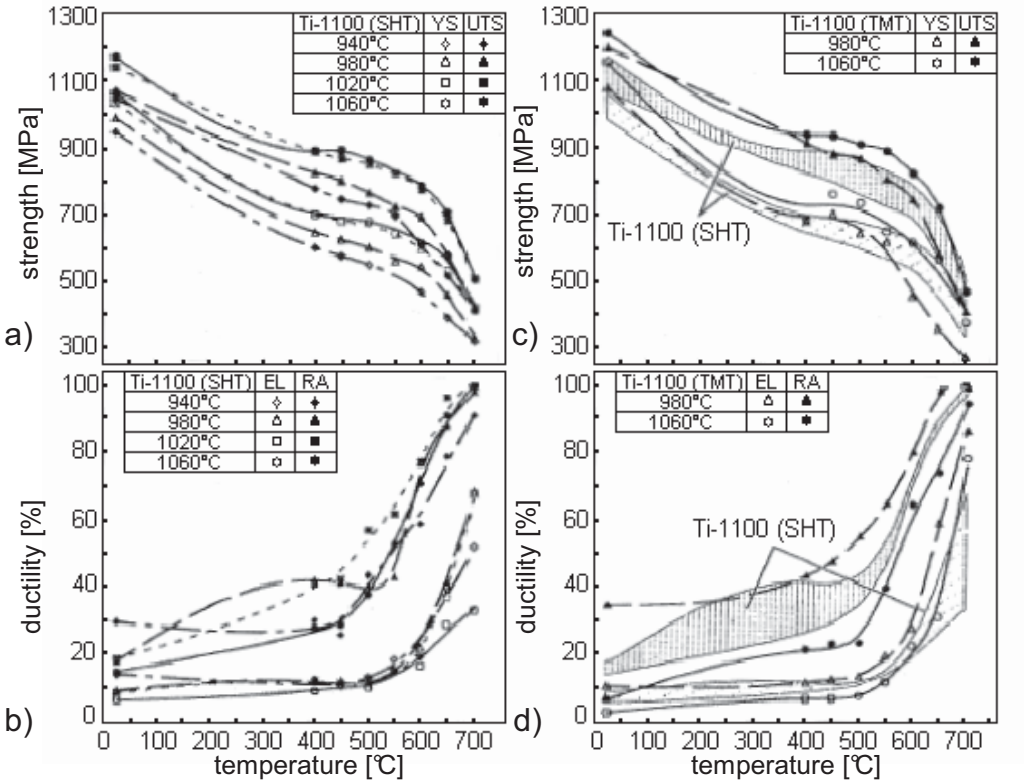

Fig. 2-13: Influence of heat-treatment temperature and thermo-mechanical heat-treatments on tensile properties of Ti-1100 [18].

2.4. Production of titanium alloys

Rutile (TiO_2) and ilmenite ($FeTiO_3$) are mainly used as sources for titanium production. Following the extended Kroll process, the oxides are reduced to titanium. The first step involves a pre-cleaning and enrichment treatment. Afterwards the actual reducing step follows, whereas, the titanium oxide is reduced to titanium tetra chloride by chlorine and further is reduced by magnesium or sodium to form the final titanium sponge. According to the chosen method, the reduction by-products $MgCl_2$ or NaCl must be removed by leaching, inert gas sweeping or vacuum distillation [5]. Purity can be increased by cycling condensation and fractionating steps.

Mainly two methods are used for the final alloy production. Both are based on at least two remelting steps to get rid of contaminants from the Krolls process and to produce ingots of high quality for mill and casting use [5].

2.4.1. Vacuum arc remelting

Pre-materials of the final alloy, precisely titanium sponge, pre-alloys (master alloys) or elements and clean scrap material, are mechanically compacted using a hydraulic press. Several of these blocks are welded together in inert gas by titanium straps, to form the first melt electrode [5]. The melt electrode is installed into the vacuum arc remelting (VAR) facility and the whole subsequent process is run in a vacuum atmosphere. The arc is ignited between the electrode and remains of swarf on the bottom of the water-cooled melting pool. The electrode now works self-consuming and the molten metal forms an ingot that is reused as an electrode in the next process step [24].

2.4.2. Hearth melting technologies

Newer methods in titanium ingot production are electron beam – cold hearth melting (EB-CHM) and Plasma-CHM. These technologies use electron and plasma guns as heat sources. For high quality production, however, a final VAR step must be added [24].

2.4.3. Forging

The ingot can obtain the final shape by various form-giving processes. Different types of forging such as open-die, closed-die, upsetting, role orbital, ring forging and forward and backward extrusion are available to realize a wide variety of desired forging shapes. The actual form-giving process often combines two or more forging types and is followed by thermal heat-treatments. This sequence of thermo-mechanical and thermal treatments can be used to tailor specifically desired microstructures and properties of the final part. Forging has typically a significant positive impact on the mechanical properties such as tensile strength, creep resistance, fatigue strength and toughness. Basically, forging can be divided into two different types: α-β-forging (below T_β) and β-forging (above T_β) [5,24].
Forging in the α-β-phase field promotes a microstructure typically characterized by deformed or equiaxed primary α-grains in a transformed β-matrix (Fig. 2-14 picture 6). The resulting microstructure has an optimal effect on the combination of strength

and ductility properties as well as on the low and high cycle fatigue properties [5,25]. Fig. 2-14 shows the schematical evolution of the typical microstructure during the α-β-forging. The α-phase and the β-phase deform simultaneously during deformation (see Fig. 2-14 pictures 1-4). The evolution of the final microstructure presented in Fig. 2-14 (picture 5-6) show, that new β-grains recrystallize on grain boundaries of former β-grains as well as within the grains and at the β-phase between the α-plates. The growth of these new β-grains is restrained by boundary α-phase formed and located at the former β-grain boundaries and within the grain, which depends on the cooling rate.

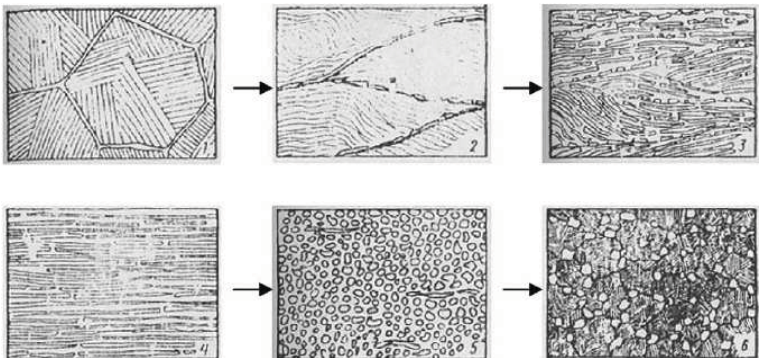

Fig. 2-14: Schematical evolution of the microstructure through forging in the α-β-phase field [25].

The second fundamental forging type is β-forging, conducted at temperatures above T_β and producing typical transformed β or acicular microstructures. The schematical development of these microstructures is shown in Fig. 2-15. First, the equiaxed β-grains elongate (1-3). By exceeding the temperature and deformation limit the dynamic recrystallization starts which leads to nucleation of recrystallized β-grains at triple junctions. Kept long enough at high temperatures will lead to a complete recrystallized microstructure of β-grains (4-5). If the temperature, however, falls below T_β before recrystallization is completed, α-grains will precipitate on defects of the original, deformed β-grains. These α-grains constrain the newly formed β-grains and form a boundary phase. Such microstructure has a positive effect on fracture toughness, fatigue crack propagation resistance, notch tensile strength and creep resistance. Nevertheless, β-forging leads to decreased strength and ductility values, in contrast to α-β-forging. Technologically, β-forging is conducted under low forging pressures and the final parts show reduced cracking tendencies compared to forging procedures below T_β. However, attention has to be carefully drawn to non-uniform working, excessive grain growth and poorly worked structures [25].

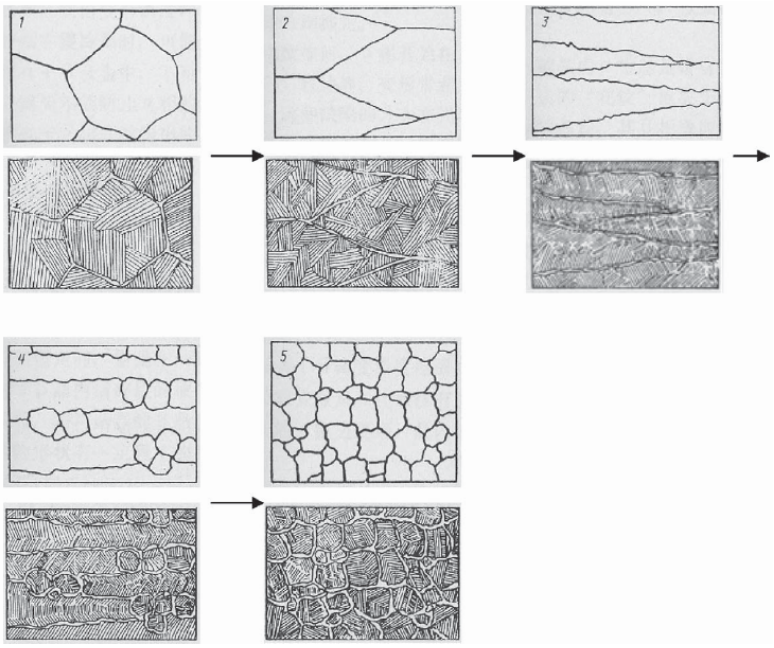

Fig. 2-15 Schematical evolution of the microstructure through forging above T_β [25].

Basically, titanium alloys show high strain rate sensitivity (e.g., see Fig. 2-10 b), meaning they show high resistance, if higher strain rates are applied. This effect can be undergone by a reduction of the rate, though a compromise must be done to avoid metal temperature loss [5].

2.4.4. Heat-treatment

Reasons for an additional heat-treatment after the form-giving process are various, indicated by the different types of treatments: stress relieving, annealing to produce optimal combination of ductility, machinability, dimensional and structural stability; solution annealing and aging to increase strength and finally desired properties, such as fracture toughness, fatigue strength and high-temperature creep strength. Still, it depends on the alloy, if the heat-treatment turns out to be useful. Annealing combined with stress relieving is an adequate treatment of α-β and near-α-alloys, though a strengthening effect can not be achieved [4]. Instead, β-alloys, for example, show a strengthening effect, due to the decomposition of metastable β. Processing of near-α-alloys above T_β can increase creep properties. On the other hand, IMI proposes processing little below T_β for alloy IMI 834, to achieve a good combination of creep and fatigue properties [4].

2.5. Oxidation

For high temperature applications, the convincing advantage of near-α-alloys is the good combination of mechanical properties and oxidation resistance. This resistance is based on the chemical composition and the adjusted microstructure. Further improvements can be done by pre-oxidation and coatings [26], but those two issues will not be discussed here.

Oxidation behavior is based on the effects of oxide scale formation and dissolution of non-metals in the subsurface zone. The scales are composed of Al_2O_3 and TiO_2. Since TiO_2 is formed by fast growing, it displays a highly disordered structure and does not provide sufficient protection [26]. Therefore, Al_2O_3 is responsible for the oxidation protection, but the quantity depends on the material composition and will not protect sufficiently below ~50 m.% of Al content [27]. Oxide scales formed on titanium base alloys as a function of the Al content are shown in Fig. 2-16.

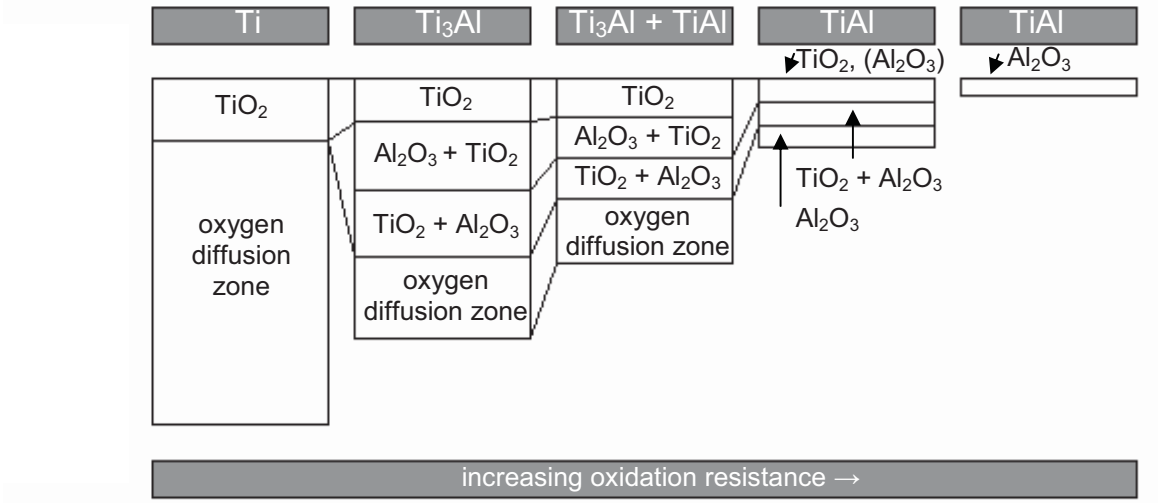

Fig. 2-16: Oxide scales and oxygen diffusion zones of titanium-base alloys as a function of the Al content [26].

The solubility of up to 33 at.% oxygen or 22 at.% nitrogen in Ti distorts the lattice and causes embrittlement. This hardened subsurface zone decreases extremely the ductility of the component and enhances crack propagation [26]. Alloying elements such as Nb and Si can improve the oxidation behavior [26]. The positive effect of 8-10 at.% Nb on the oxidation resistance was shown for γ-TiAl and α_2-Ti_3Al based alloys [26]. At higher contents, the benefits of Nb inverse [27]. This inverse effect was shown on Ti-(22-25) Al-xNb (at.%) alloys by Leyens and Gedanitz [28]. Benefits are based e.g. on the formation of a stable Ti-rich layer at the interface between oxide and metal, enrichment of Nb below the oxide scale and the reduction of oxygen

solubility in the alloy. A similar positive effect of the 0.7 m.% of Nb in IMI 834 could not be shown as for the Nb-free Ti-1100, since the content is way below the content named before [29].

Investigations made on the recommended microstructures of Ti-1100 and IMI 834 have provided evidence concerning the important influence of the microstructure [29]. IMI 834 with its recommended bimodal microstructure shows a slightly better oxidation resistance than the lamellar Ti-1100. The comparison between both alloys is shown in Fig. 2-17 and demonstrates that the oxidation resistance increases strongly by changing from bimodal to lamellar structure. Furthermore, Fig. 2-18 displays the dependence of weight gain on temperature for IMI 834 and Ti-1100. With increasing temperatures, a higher weight gain can be noticed. The dependence of the weight gain for IMI 834 and Ti-1100 can be described by a parabolic law [18] as shown in Fig. 2-17 and Fig. 2-18.

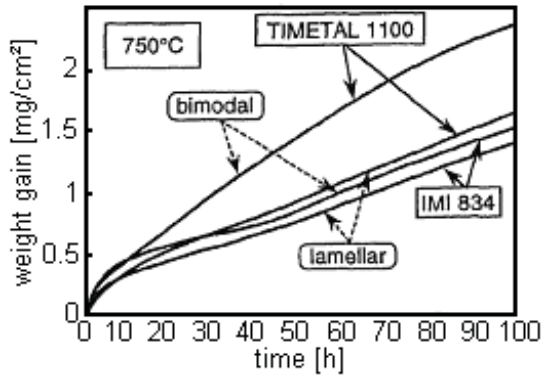

Fig. 2-17: Comparison of the oxidation resistance of IMI 834 and Ti-1100. Both are represented in bimodal and lamellar microstructure [26].

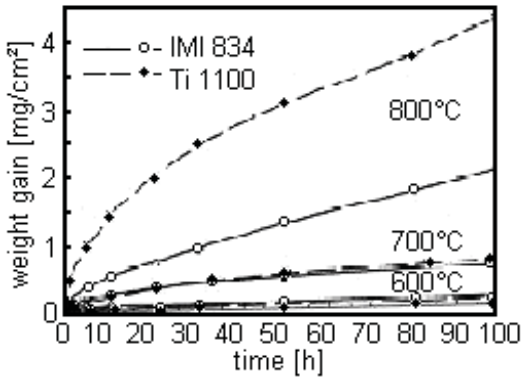

Fig. 2-18: Comparison of weight gain of the bimodal IMI 834 and the lamellar Ti-1100 at different oxidation temperatures [18].

Fig. 2-18 points out that above 600℃ IMI 834 and Ti-1100 show a decrease in oxidation resistance and, thus, a tremendous increase in weight gain [9]. At temperatures above 750℃, Ti_3AlN occurs as a new phase at the interface between the substrate and the oxide, accompanied by weakening the adherence of the oxide scale [9].

3. Material and experimental methods

3.1. Tested material

NB4, named after its characterizing element niobium, has the nominal chemical composition as listed in Tab. 3-1. It also shows the result of the chemical analysis of head and bottom of the ingot.

Tab. 3-1: Nominal chemical composition and the composition range of an ingot of alloy NB4 in m.%. The first value was obtained at the head section, the second at the bottom section of the triple-melted VAR ingot.

	Ti	Al [m.%]	Nb [m.%]	Mo [m.%]	Si [m.%]	O [ppm]
nominal	bal.	9	4	0.5	0.5	1800
ingot	bal.	9.05 - 9.25	4.05 - 4.3	0.51 - 0.55	0.49 - 0.52	1800

In a study prior to this work the composition was chosen in the course of a joint project between DaimlerChrysler AG and the Department of Physical Metallurgy and Materials Testing of the University of Leoben. Systematic thermo-dynamic calculations were conducted by MatCalc using a commercially available database [30,31] in order to define a potential alloy. These calculations enabled the prediction of common phases and their fractions of the alloy NB4 at different temperatures, as presented in Fig. 3-1. The tested material of this diploma thesis has an oxygen content of 1800 ppm, which, however, changes the phase fractions only slightly.

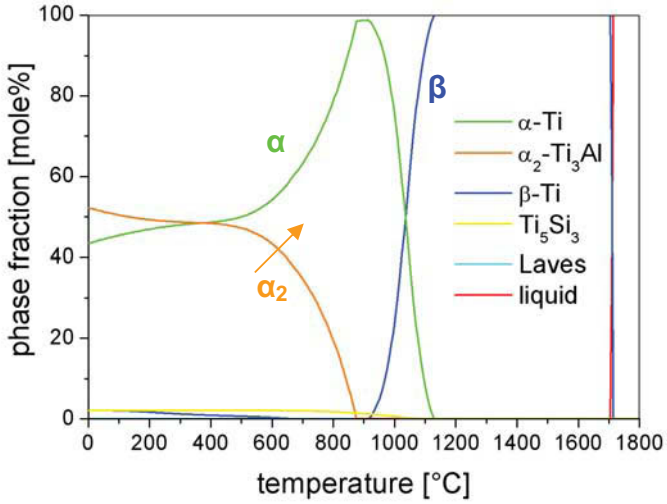

Fig. 3-1: Thermo-dynamical calculations of the phases presented in a NB4 alloy with an oxygen content of 1800 ppm. Increasing the oxygen content would move the α_2-curve to higher α_2-contents (see arrow).

The samples can be divided into different conditions: extruded material, which will be called large cross-section material (LCS) and valve blanks, which are subclassified into 3 variants: version S (VBS) is forged 30℃ abo ve T_β, variant U (VBU) is forged 30℃ below T_β and version T (VBT), an extended version of VBU, which is additionally heat-treated 30℃ above T_β as illustrated in Fig. 3-2.

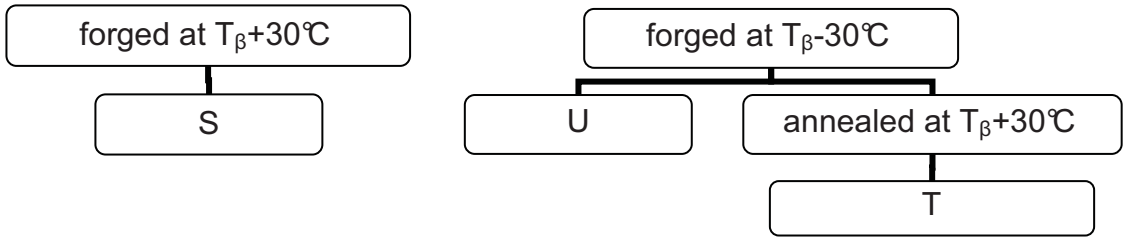

Fig. 3-2: Classification of the investigated valve blanks.

A section of a valve blank is shown in Fig. 3-3 and positions of interest are indicated.

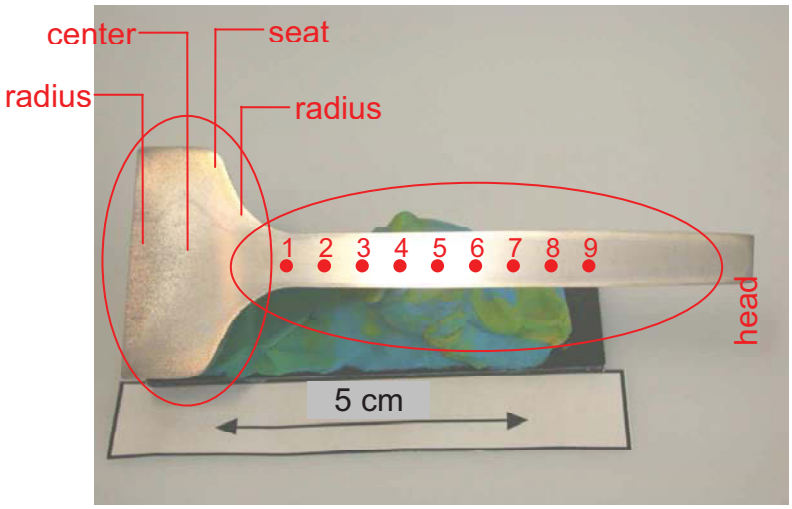

Fig. 3-3: The investigated positions are indicated by 1 to 9 on a forged valve blank section.

The ingot was produced by a triple VAR process by GfE (Gesellschaft für Elektrometallurgie), Nürnberg, Germany. Subsequently, the ingot was turned and coated with glass to obtain better friction conditions for the following extrusion process. A rod with a length of 16 m and a diameter of 35 mm was extruded and subsequently cooled in water. This is now the raw material for the upcoming form-giving process of the valve blanks.

For the forthcoming heat-treatments, the exact T_β was determined as 1037°C by means of DSC measurements, which were provided by GfE and shown in Fig. 3-4.

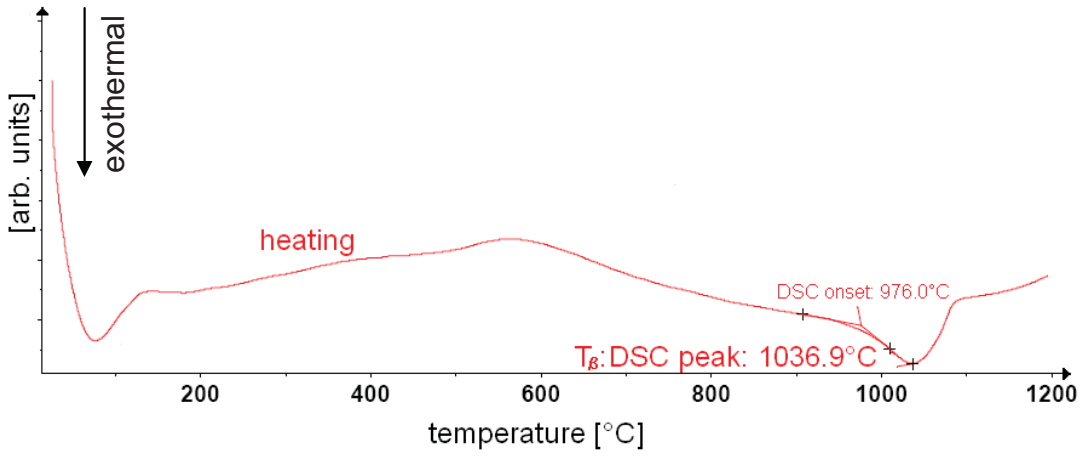

Fig. 3-4: Results of DSC measurements conducted on NB4 in LCS condition with a heating rate of 20 $Kmin^{-1}$. The β-transus temperature is defined as the exothermal peak at 1037°C.

Prior to the form-giving process, conducted by Forge de Bologne, France, the surface of the LCS material was turned down to a diameter of 30 mm and cut into parts of an approximately length of 55 mm. After preheating the performs for 20 minutes, the material was forged at T_β+30℃ or T_β-30℃ using preheated forging dies. The final form-giving process was a combination of extruding and forging and lasted about 2-3 seconds. Subsequently, the forged parts were quenched into water within a transfer time of maximum 10 seconds.

3.2. Analysis of the microstructure and heat-treatments

All samples were mechanically ground, starting with P120 sand paper up to P4000 as shown in Tab. 3-2. Every individual grain size cycle lasted at least 3 minutes with a pressure indicated in Tab. 3-2. Polishing was completed using a 3 µm grain size disk followed by final polishing. Every polishing cycle lasted 6 minutes applying a pressure of 1.5 bar. Finally, the samples were cleaned with ethanol and dried by a blow dryer.
For light optical investigations, the samples were edged using the method of Kroll [32].

Tab. 3-2: Schedule of metallographical sample preparation for microstructure analysis.

		time	pressure
grinding	P120	3 min	2 bar
	P320	3 min	1.5 bar
	P800	3 min	1.5 bar
	P1200	3 min	1.5 bar
	P2500	3 min	1.5 bar
	P4000	3 min	1.5 bar
polishing	3 µm	6 min	1.5 bar
	final polishing	6 min	1.5 bar

Besides characterization of the initial microstructure of LCS material and valve blank versions VBS, VBT and VBU, samples with additional heat-treatments (HT) as listed in Tab. 3-3 and Tab. 3-4 were characterized. The microstructure characterizations were focused on the influence of temperature, time and working conditions.
Heat-treatments were conducted in laboratory air furnaces. First, they were heated to the required annealing temperature. An additional soaking time of 10 minutes was added to the annealing time as indicated in Tab. 3-3 and Tab. 3-4. In order to obtain

a uniform air cooling, the samples were placed on a fibrous mat of Nextel 312 3M. The quenched samples were cooled down in water (22°C) within approximately 3 seconds.

Tab. 3-3: Schedule of characterized microstructures of LCS material used for microstructural investigations.

LCS						
	HT 1	time 1	cooling 1	HT 2	time 2	cooling 2
influence of temperature	650℃	14h	AC			
	750℃	14h	AC			
	850℃	14h	WQ			
influence of time	1010℃	20 min	WQ			
	1010℃	30 min	WQ			
	1010℃	1h	WQ			
	1010℃	2h	WQ			
influence of working temperature	650℃	8h	AC	800℃	8h	WQ
	800℃	8h	WQ	800℃	8h	WQ
	850℃	8h	WQ	800℃	8h	WQ
long time influence	650℃	24h	AC			

Tab. 3-4: Heat-treated VBS material used for metallography and phase analysis.

VBS				
	HT 1	time 1	cooling 1	position
influence of temperature	650℃	2h	AC	stem
	750℃	2h	AC	stem
	850℃	2h	WQ	stem
phase analysis	650℃	14h	AC	stem
	800℃	8h	WQ	stem

3.3. Hardness tests

Brinell hardness tests were conducted on LCS material and VBS stems, initial material as well as heat-treated samples, according to DIN EN ISO 6506-1. The tests of LCS material were conducted on discs of about 0.7 mm thickness, which were cut from the extruded rod and divided into half. According heat-treatments were performed over a time range from 1 h up to 14 h at a temperatures scale from 650℃

to 850℃ as listed in Tab. 3-5. Hardness measuremen ts were conducted, before and after annealing on both sides, as illustrated in Fig. 3-5. Before running the hardness tests, the samples were ground up to P1200. In case of heat-treated samples, the oxide layer was removed at first.

The stem of the VBS material was cut into little cylinders as shown in Fig. 3-6. Hardness testing was conducted on both cross-sections. Again, the surfaces have been ground up to P1200, and in case of heat-treated samples, a sufficiently thick layer of material was removed to satisfy a valid hardness test. Every cylinder was tested at initial conditions and after heat treatments, as scheduled in Tab. 3-5. All heat treatments finished with an air cooling procedure.

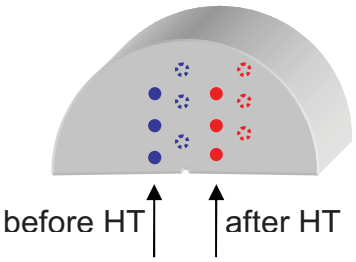

Fig. 3-5: Typical sample for hardness tests conducted on LCS material.

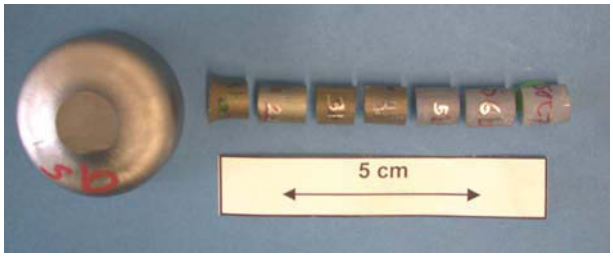

Fig. 3-6: Samples for hardness tests taken from a VBS stem.

Tab. 3-5: Heat-treatments performed on LCS and VBS material, which was subjected to Brinell hardness tests.

	1h		2h		4h		8h		14h	
600℃	LCS	---	LCS	---	LCS	---	LCS	---	LCS	---
650℃	LCS	VBS	LCS	VBS	LCS	VBS	LCS	---	LCS	VBS
700℃	LCS	---	LCS	---	LCS	---	LCS	---	LCS	---
750℃	LCS	VBS	LCS	VBS	LCS	VBS	LCS	---	LCS	VBS
800℃	LCS	---	LCS	---	LCS	---	LCS	---	LCS	---
850℃	LCS	VBS	LCS	VBS	LCS	VBS	LCS	---	LCS	VBS

3.4. Tensile tests

All tensile samples were manufactured by Metalax Eisele, Neustadt, Germany. In case of the annealed LCS material, cylinders were eroded from the rod. The LCS was first heat-treated and finally machined. For the preparation of tensile samples of

heat-treated valve blanks, the stems were separated from the head, annealed and turned into the final shape.
For LCS material round samples according to DIN 50125 Form B – M10 were used. Valve blanks were turned into samples according to DIN 50125 Form B – M8.

3.4.1. Tensile tests at room temperature

All tensile tests at room temperature were conducted by the Esslingen University of Applied Sciences. Room temperature tensile tests were conducted according to DIN EN 10002-1.

3.4.2. Tensile tests at elevated temperatures

All tensile tests at 600℃ and 800℃ were performed by the Mechanical Testing Laboratory of DaimlerChrysler in Ulm, according to EN10 002-5. Heat treatments were chosen for valve blanks, based on the results of LCS material.

3.5. Dilatometry and deformation tests

3.5.1. Sample preparation

Cylindrical samples (ø 4 mm, length 10 mm) were eroded from the LCS material parallel to the direction of extrusion, as shown in Fig. 3-7. A thermocouple was spot-welded onto the middle of the sample, another one on the end close to the top-surface (see Fig. 3-8). The thermocouple in the middle is used for temperature control, whereas, the second one controls the uniformity of the temperature over the length of the sample. Both thermocouples are of the Pt/PtRh type. Mo plates of a diameter of 7 mm were fixed with super glue on both ends of the samples in order to decrease heat transfer between sample and dilatometer die.

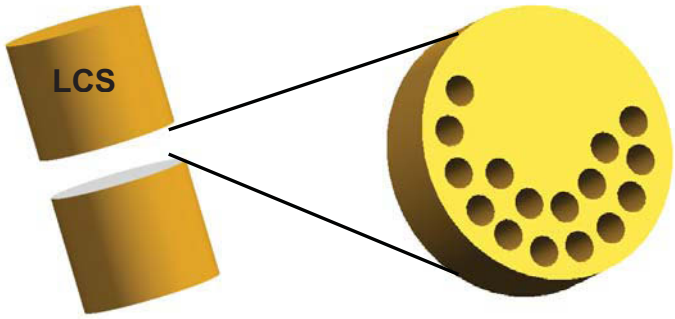

Fig. 3-7: Schematic depiction how dilatometry samples were taken from the LCS material.

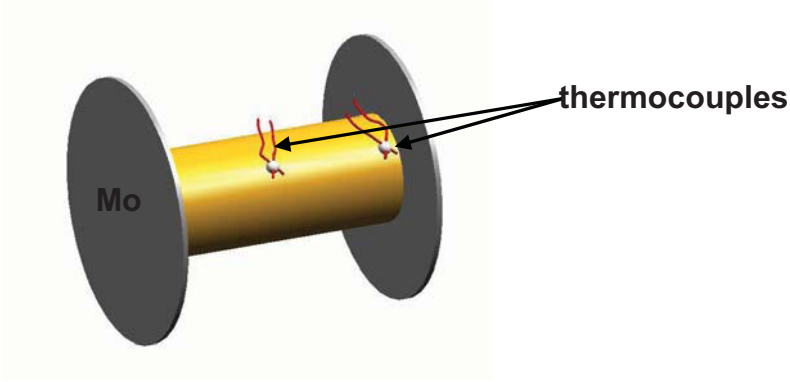

Fig. 3-8: Fixation of thermocouples and Mo plates on a sample, which is used for deformation tests in a dilatometer.

Every sample was assembled in the dilatometer and was centered in a heating coil. Displacement transducers made of alumina were used, which also provided the force of deformation.

3.5.2. Experimental details

The tests were performed with the Dilatometer DIL 805A/D of the German Baehr company. Tab. 3-6 displays the schedule of parameters of the deformation tests. First, the sample was heated up to deformation temperature in an inductive heating coil. Half of the total samples series were subsequently water quenched, whereas samples of the second series were first air cooled for 5 seconds and finally water quenched. The second version better simulated the production process, because the transfer time of the forged valve blank to the water basin takes about 5 seconds. Three of the samples were deformed at the same temperature (50℃ above T_β), but with different deformation speeds. Both the remaining samples were deformed at the maximum speed, one at 30℃ above T_β, the other one at 70℃ above T_β. All samples

were deformed up to a deformation degree of 0.7, which corresponds to a reduction in size of 50 %.

To guarantee a uniform heating, the process was done in steps of different heating rates, as shown in Fig. 3-9. After holding at the final temperature for 90 s, the deformation step takes place, subsequently followed by the cooling, depending on the chosen setting.

Tab. 3-6: Deformation and subsequent cooling parameters used for LCS material.

sample	temperature	deformation speed	deformation degree φ	cooling
cooling condition 1				
1	1090℃	1 mm/s	0.7	WQ
2	1090℃	10 mm/s	0.7	WQ
3	1090℃	100 mm/s	0.7	WQ
4	1070℃	100 mm/s	0.7	WQ
5	1110℃	100 mm/s	0.7	WQ
cooling condition 2				
6	1090℃	1 mm/s	0.7	5 s AC → WQ
7	1090℃	10 mm/s	0.7	5 s AC → WQ
8	1090℃	100 mm/s	0.7	5 s AC → WQ
9	1070℃	100 mm/s	0.7	5 s AC → WQ
10	1110℃	100 mm/s	0.7	5 s AC → WQ

Heating-up to 200℃ was done within 3 minutes. At t he same time, the vacuum pump was switched on. The second heating section, up to 1050℃, simultaneous with flushing the sample chamber with helium, lasted 14 minutes. Two minutes were scheduled to heat up to final deformation temperature, where the temperature was hold for 90 seconds. Then the deformation step followed at a selected speed. For cooling condition 1, a cooling rate of 11.2 K/s was chosen. For the second condition, the first cooling rate was 8.6 K/s, which represents air cooling followed by a cooling rate of 10.8 K/s, which corresponds to water quenching.

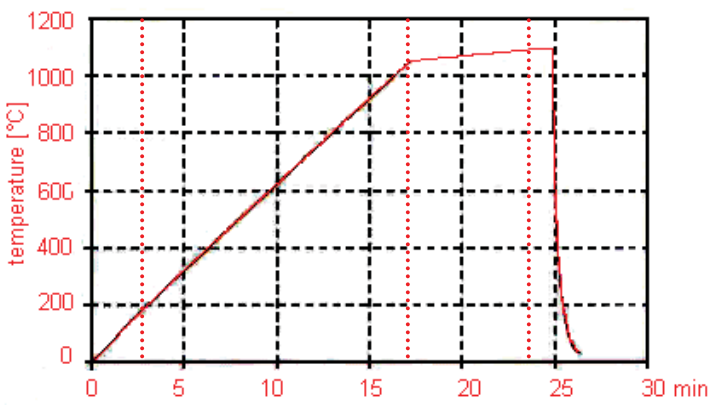

Fig. 3-9: Plot of a heating and cooling curve during a deformation test.

After the test, the deformed sample was cut into two (parallel to the direction of deformation) for microstructural analysis according to chapter 3.2.

3.6. Phase analysis

To characterize the presence and quantity of the different phases, a variety of different methods was used, which are described in the following chapters in detail.

3.6.1. Quantitative phase analysis

Sample preparation was done as given in chapter 3.2 and images with a magnification of 500 were taken by means of a light-optical microscopy. The pictures were edited by ANALYSIS© by setting the shading correction and the threshold of colors.

3.6.2. X-ray diffractometry

The surface of samples was prepared as given in chapter 3.2 and analyzed employing a Siemens Kristalloflex D500. A voltage of 40 keV and a current of 30 mA were used to generate a CuK_α beam with a wavelength of $\lambda = 1.542$ Å. Typical θ-2θ spectra were measured and final phase fraction calculations were done by a Rietveld analysis using the software package of TOPAS© [34].

3.6.2.1. Rietveld

Based on the x-ray diffraction (XRD) spectrum, the Rietveld refinement method offers the possibility to determine the quantities of the present phases. The measured XRD

spectrum can be described by analytic functions, which are adapted by the method of least squares. This adaptation of the parameters, namely the position of the peaks, integral intensity, half heights width, form of edges and asymmetry, is done repeatedly again to improve the matching of the calculated curve. Since this method needs a starting function, there is a source of insecurity. To decrease the dependence of the result on the starting model, the software TOPAS©, commercialized by the company Bruker-AXS, uses the method of fundamental functions. By considering the distribution of intensity of the x-ray source versus wave length and system specific parameters, such as length and width of the aperture slot x-ray patterns are calculated [33].

3.6.3. Scanning electron microscopy

The scanning electron microscopy (SEM) investigations were conducted with a Zeiss Evo 50 system on the same samples as for XRD measurements. Images were taken in the back scattering (BSE) mode and electron back scattering diffraction (EBSD) measurements were conducted employing an Oxford Inca Crystal 300 system. An acceleration voltage of 20 kV was chosen.

3.6.4. Transmission electron microscopy

Discs of a diameter of 3 mm were cut from the material and thinned by grinding and polishing up to P4000 to a thickness of 100-110 µm. Subsequent concentrically grinding by the Dimple Grinder Model 656 of Gatan leads to a dimple depth of 20 µm. The first two thirds of these dimpling processes were ground with a 15 µm suspension; the last third was ground with a 6 µm suspension down to 30 µm thickness and a 1 µm suspension to the final depth of 20 µm. The final preparation was done by ion polishing using the Precision Ion Polishing system 691 of Gatan. Beam energy was chosen to be 3.7 keV and was decreased during the final steps to 3 keV. It operated with two guns and the rotation speed was 3 rpm until the appearance of a small hole was detected.

3.7. Oxidation experiments

For these investigations, valve blanks of different alloys and microstructure conditions were used. Valve blanks of NB4 in S, T and U version as well as alloy NB7 and Alloy 2, alloys of similar composition as NB4 but with different contents of Nb, were studied. In addition, material taken from a valve made of IMI 834 was

characterized. The nominal chemical compositions of all tested materials are given in Tab. 3-7.

Tab. 3-7: Nominal chemical composition of oxidation tested near-α-alloys.

	Ti [m.%]	Al [m.%]	Sn [m.%]	Zr [m.%]	Nb [m.%]	Mo [m.%]	Si [m.%]	O [ppm]
NB4	bal.	9	---	---	4	0.5	0.5	1800
NB7	bal.	9	---	---	7	0.5	0.5	---
Alloy 2	bal.	9	---	---	0.5	0.5	0.5	---
IMI 834	bal.	5.8	4	3.5	0.7	---	0.35	---

Cylindrical samples - 3 mm in diameter and 1 mm in height - were machined parallel to the stem axis. All oxidation experiments were conducted in the DSC/TG instrument Setsys Evolution of Setaram.

4. Results and discussion

4.1. Analysis of the starting microstructures

4.1.1. LCS material

The large cross section material is the first to characterize. It shows an equiaxed grain structure with a grain size of about 200 µm (Fig. 4-1 and Fig. 4-2). The grain size decreases from the center to the edge of the extruded rod. The large grains are surrounded by a fine grain boundary phase. In the longitudinal direction, parallel to the extrusion direction, the LCS material shows unrecrystallized sections that run through the whole material and could be seen bare-eyed, as typically observed for extruded materials.

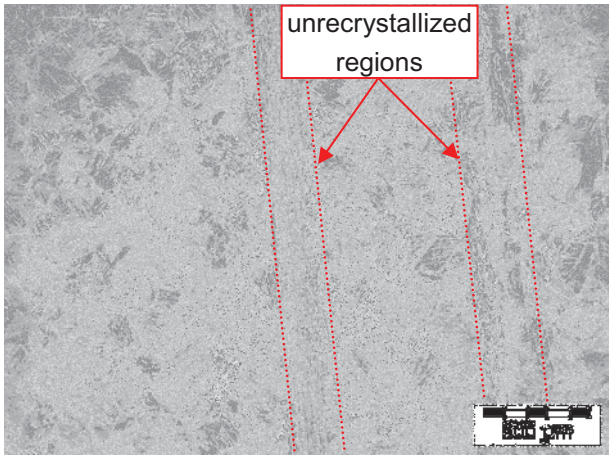

Fig. 4-1: Light optical image of the longitudinal cross section of the LCS material. In the longitudinal direction of the extruded rod unrecrystallized regions can be seen (arrows) [39].

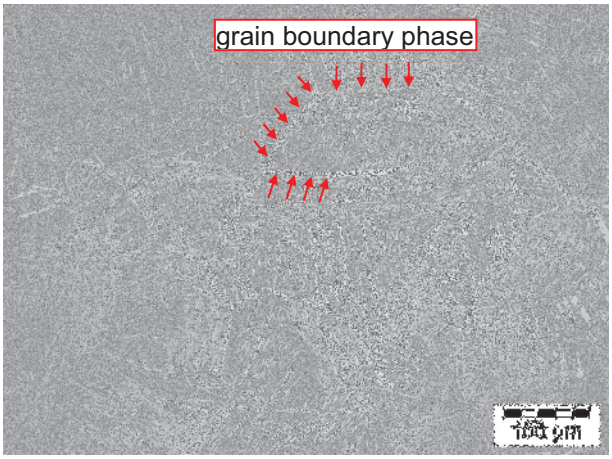

Fig. 4-2: Transversal cross section of LCS material without heat-treatment. Equiaxed grains with a lamellar structure and a grain boundary phase are present (arrows).

Similar microstructures were observed for other near-α-titanium alloys. Wanjara et al. [20] reported a microstructure of transformed β-grains with a fine acicular, martensitic or Widmanstätten microstructure. Grain boundaries of former β-grains were covered with lenticular α-phase.

4.1.2. Material in VBS condition

Depending on the local degree of deformation of the valve blank head, different microstructures can be observed. Fig. 4-3 a) shows the microstructure at the bottom of the valve blank head, which is the section with the lowest deformation. This explains the structural similarity to the microstructure of the LCS material, which is used as prematerial for valve production. The material of the center and seat position appears strongly deformed, as shown in Figs. 4-3 b) and c). The microstructure of the center position looks very deformed as well; grain boundaries and individual lamellae are broken into fragments. In the seat position, grain boundaries are not distinguishable anymore with light optical microscopy. The radius, which is the transition region from stem to head, suffers highest deformation, as shown in Fig. 4-3 d). It reveals a very fine-grained microstructure, caused by dynamic recrystallization. The grain size is reduced to about 10 µm.

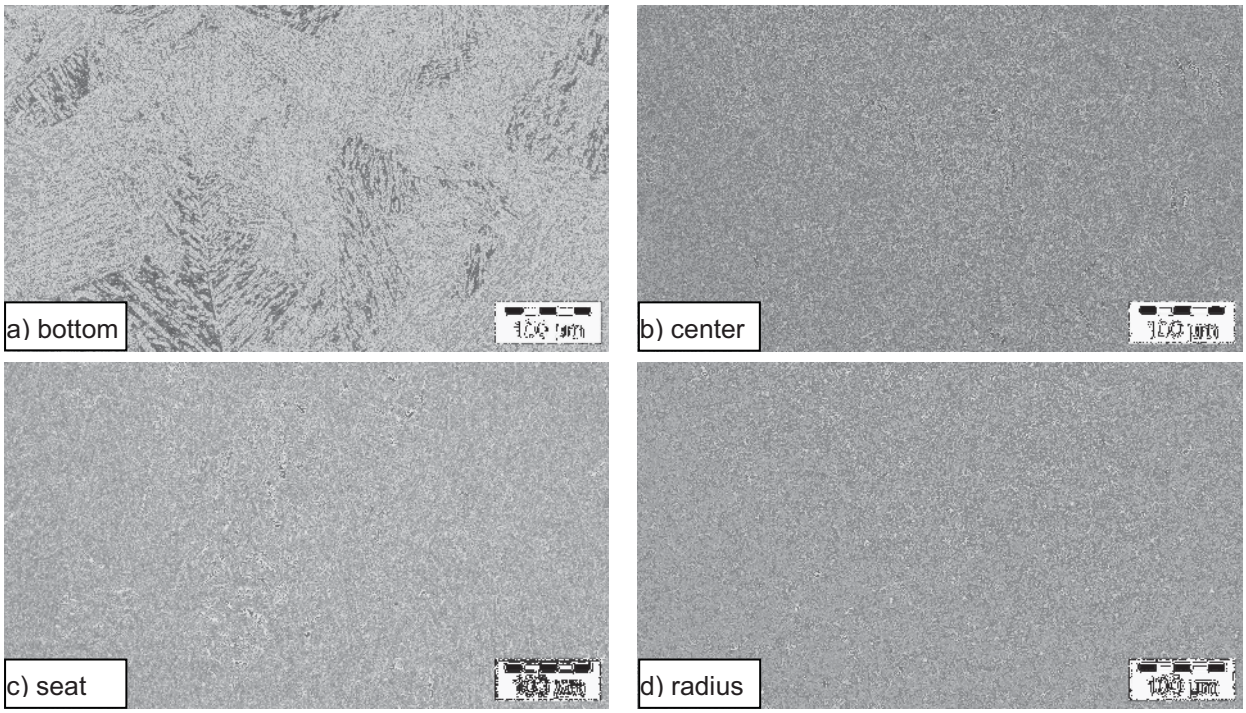

Fig. 4-3: Light optical images of the microstructure of the valve blank in VBS condition from different positions: a) bottom, b) center, c) seat, d) radius of the valve blank (see also Fig. 3-3).

During processing of the valve blank, the stem suffers highest deformation, hence, dynamic recrystallization can be observed. Fig. 4-4 displays the development of the microstructure from the stem position 1 to position 4. The microstructure of the stem starts with fine equiaxed grains of a mean size below 20 µm (position 1, Fig. 4-4). Again, the grains show a lamellar microstructure and are surrounded by a grain

boundary phase. By going to the right in Fig. 4-4, meaning along the stem, away from the head, the grain size increases, but the lamellar structure can only be resolved in the immediate vicinity of grain boundaries. In general, this vanishing of the lamellar microstructure was observed for all light optical investigations of the stems.

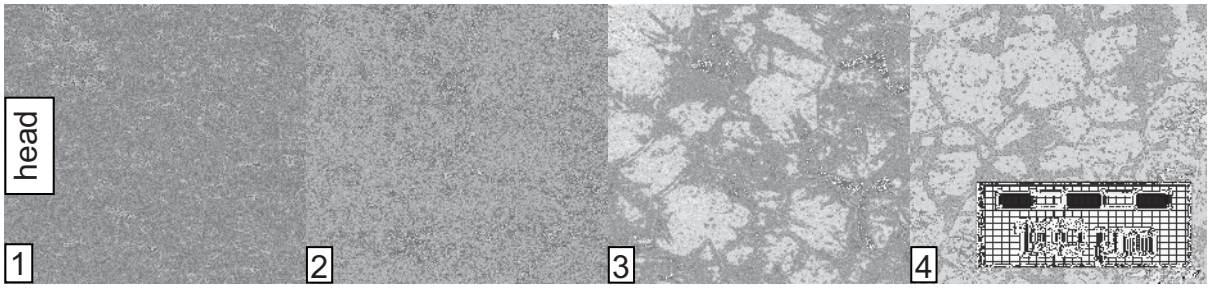

Fig. 4-4: Light optical images of positions 1-4 of the stem of a VBS valve blank (see Fig. 3-3).

4.1.3. Material in VBU condition

The main difference between the previously discussed VBS and the VBU material is the different deformation temperature (below $T_ß$). The microstructures achieved for the valve blank of the U version are very similar to the ones described in Fig. 4-4, though this version looks more filigree. Fig. 4-5 shows the microstructure at different positions of the valve blanks head and Fig. 4-6 position 1 to 4 of the stem. The structure of the lamellae and grain boundaries appears finer compared to VBS material. At the edge of the valve blanks head, the microstructure does not seem recrystallized yet. A possible reason can be the lower deformation temperature. Another difference on sight is the smaller grain size of the grains in the stem (Fig. 4-6). Again, the grain size increases, but still starts below 10 µm.

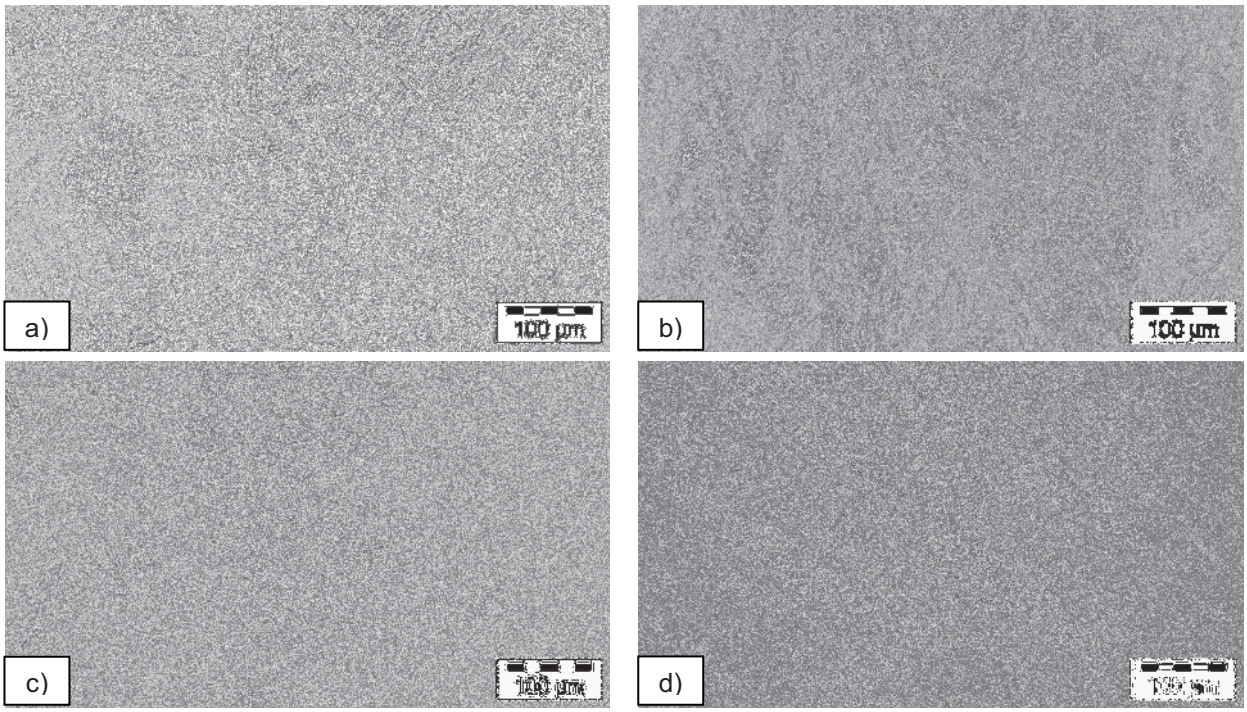

Fig. 4-5: Light optical images of the VBU material at different positions of the valve blank: a) bottom, b) center, c) seat and d) radius.

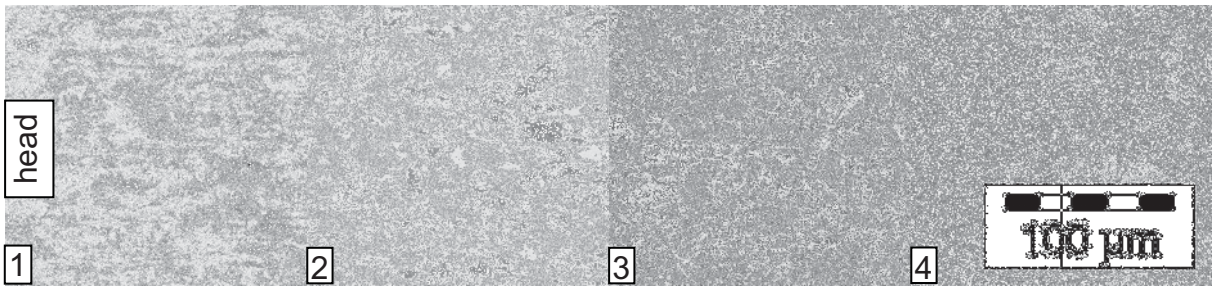

Fig. 4-6: Light optical images of positions 1-4 of the stem of a VBU valve blank (see Fig. 3-3).

4.1.4. Material in VBT condition

This variant completely differs to the previous valve blanks, because of the additional heat-treatment above T_β, which was done after the deformation process below T_β. The bottom and center of these blanks still show grains of the same size, but the lamellar structure and the grain boundary phase changed, as shown in Fig. 4-7. The previous continuous grain boundary phase split up and appears dissolved and spheroidized. The lamellar structure looks less ordered, martensitic and is intersected by broad needles. The microstructure of the strongly deformed seat and radius could barely be resolved by optical light microscope. It appears to be the same effect as seen before of the quasi-vanishing microstructure of the stem for VBS and VBU. Only at the borders of the former grain boundary phase can a needle-like microstructure

be observed, the remaining microstructure of the grain appears featureless. A closer look on the microstructure of the bottom and position 1 of the stem is presented in Fig. 4-8.

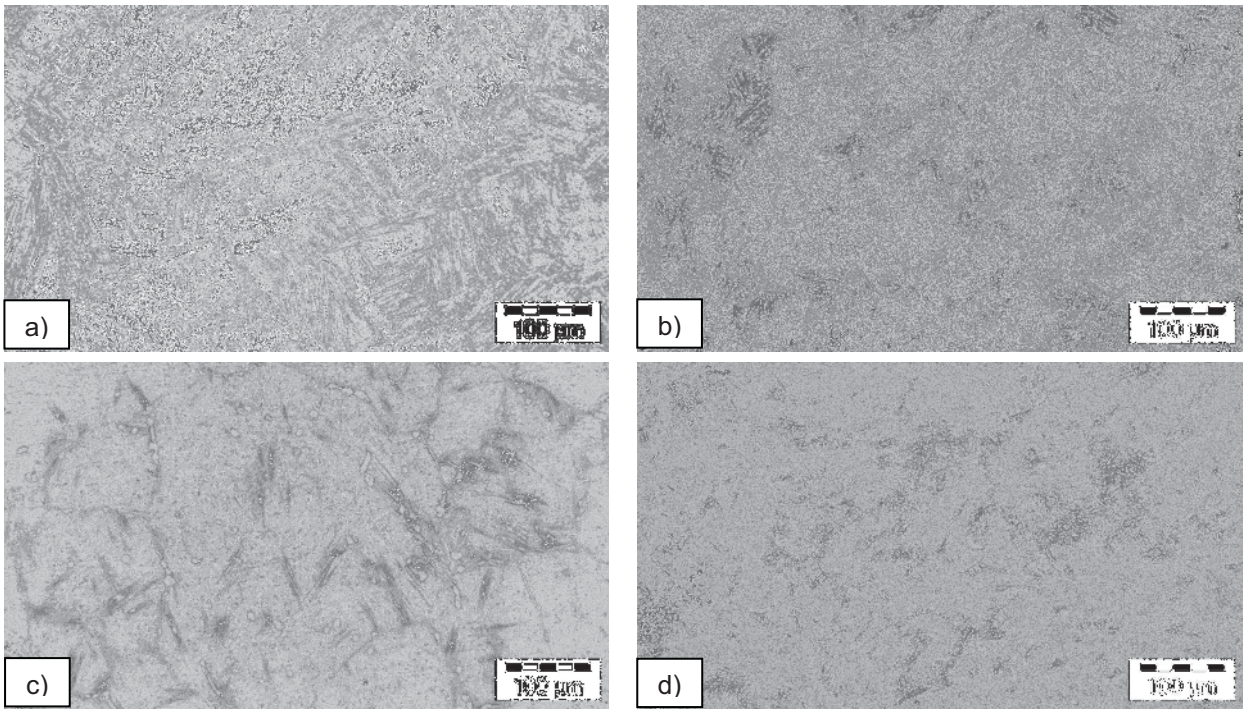

Fig. 4-7: Light optical images of the VBT material at different positions of the valve blank: a) bottom, b) center, c) seat and d) radius.

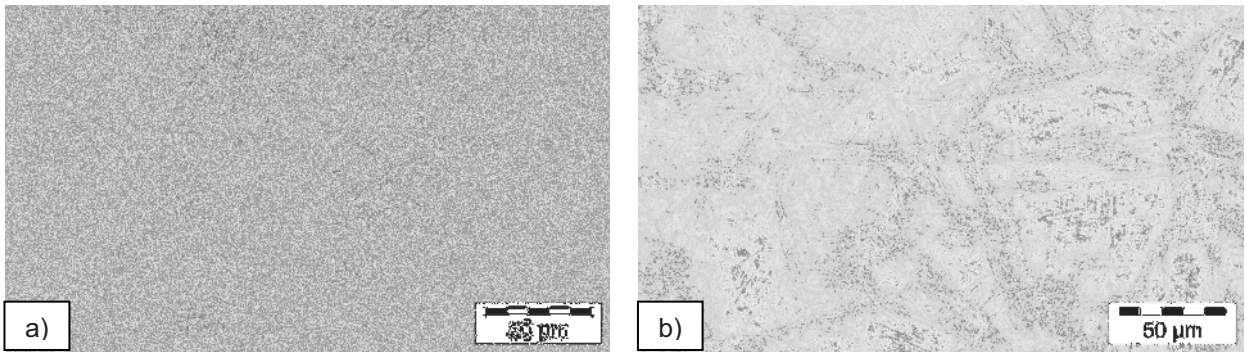

Fig. 4-8: Light optical images of VBT material at different positions of the valve blank in higher magnification: a) bottom and b) position 1.

The microstructure of the stem, considering the smaller magnification in Fig. 4-9, reveals a clearly larger grain size. Close to the head, the grain size is about 100 µm, but interrupted by a few grains larger than 300 µm. The grain size increases, by moving from position 1 to 4 to a mean diameter of about 500 µm. In Fig. 4-8 b), showing position 1, only parts of the former boundary phase can be noticed.

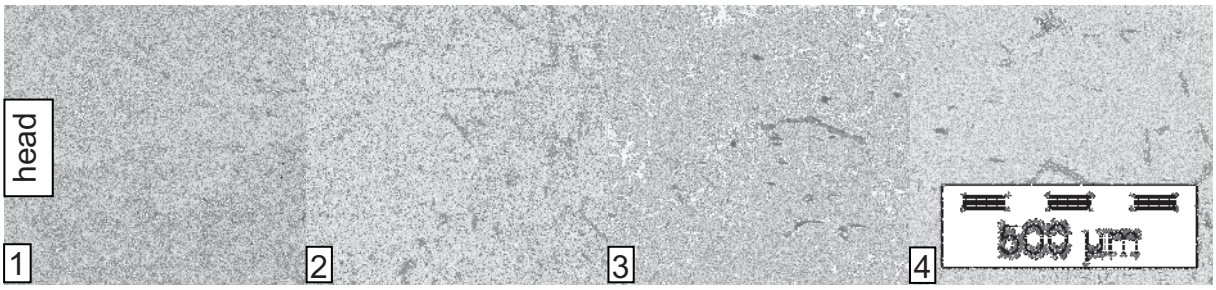

Fig. 4-9: Light optical images of positions 1-4 of the stem of a VBT valve blank (see Fig. 3-3).

4.1.5. IMI 834

Since the alloy NB4 was designed to substitute IMI 834, a valve blank made of this material was investigated in this work. The microstructure consists of equiaxed primary α-Ti and transformed β-grains, as shown in Fig. 4-10 for the head and in Fig. 4-11 for the stem. The grain size does not exceed 20 µm and is homogeneously distributed over the whole cross-section of the stem. This microstructure is already present in the head of the valve close to the stem, radius and seat (see Fig. 3-3). In the bottom of the head, original β-grains are represented by a lamellar microstructure of acicular α-grains. In fact, the microstructure is very homogenous in a valve made of IMI 834.

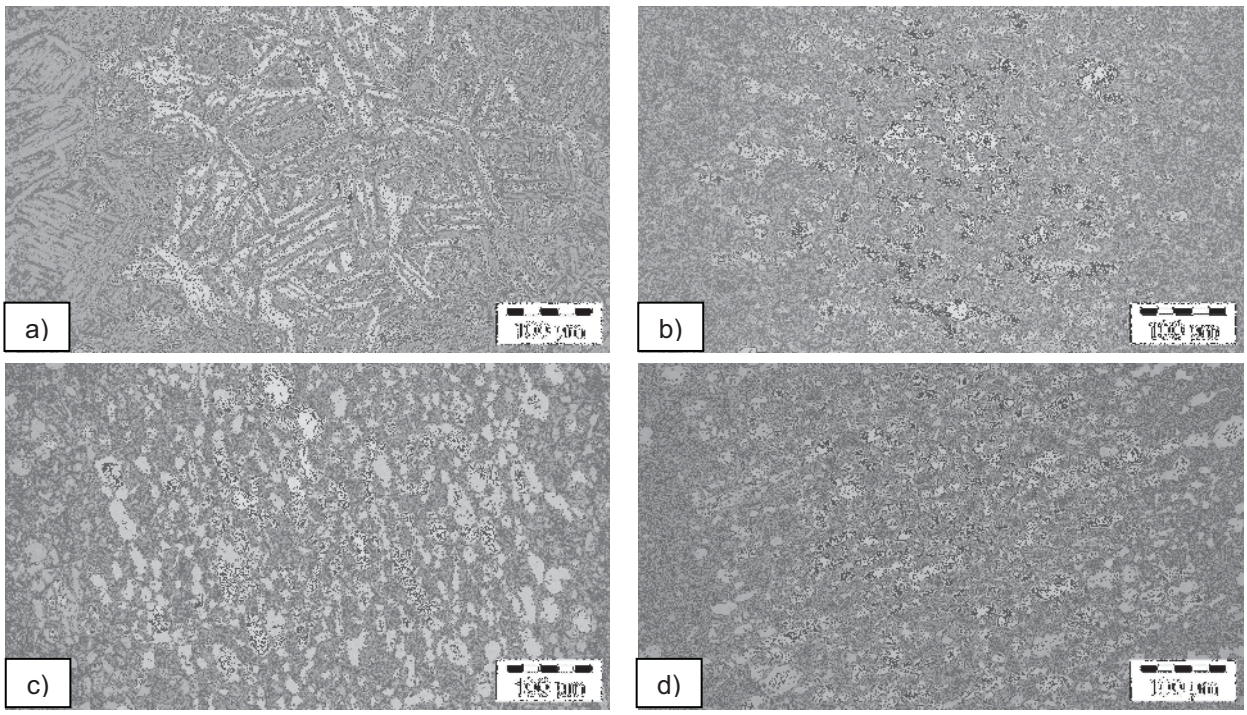

Fig. 4-10: Light optical images of the IMI 834 material at different positions of the valve blank: a) bottom, b) center, c) seat and d) radius.

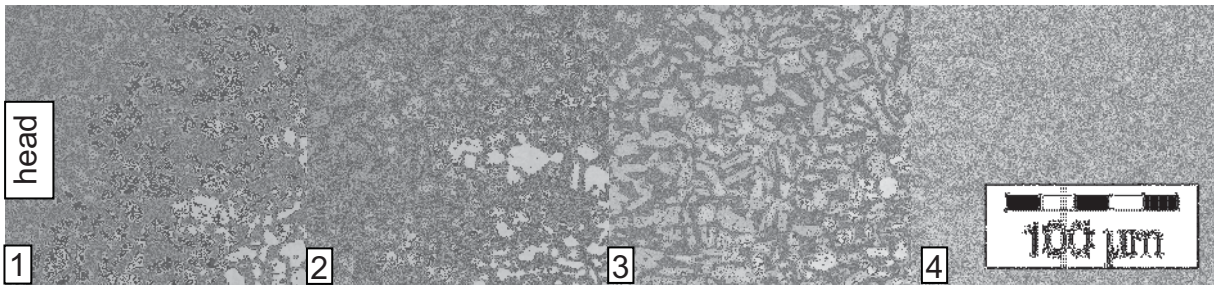

Fig. 4-11: Light optical images of positions 1-4 of the stem of an IMI 834 valve (see Fig. 3-3).

4.2. Hardness tests

The change in Brinell hardness, as shown in Fig. 4-12 for LCS material and Fig. 4-13 for VBS material, varies in response to the heat-treatments, which differed in time and temperature. Both forged states present a clear dependence of the hardness on the deformation temperature. For LCS material, the highest increase in hardness after a 14 h heat-treatment at 650℃ was detected. For all annealing temperatures, longer holding times achieve higher hardness. The beneficial effect of the heat-treatment decreased at higher temperatures, however, positive values are obtained up to 850℃. A heat-treatment below 650℃ exhibits no significant effect on the hardness change.

In order to verify the results in hardness change of LCS material, similar tests were run on VBS material and showed the same tendencies. Again, the highest increase in hardness was observed at 650℃ and followed by a decrease for higher annealing temperatures. A heat-treatment at 850℃ offered even a negative change in hardness. The benefit of long soak could not been proved, but is likely the same as for the LCS material. The negative effect of high temperatures is enforced by longer annealing times.

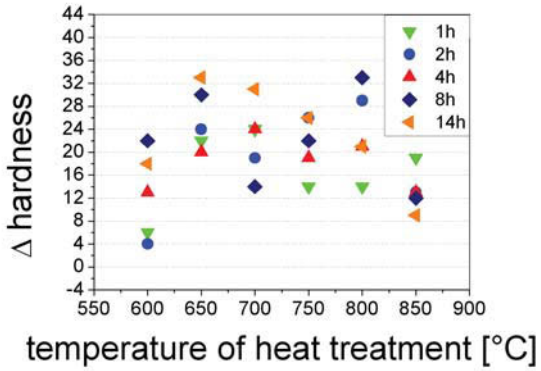

Fig. 4-12: Hardness change of LCS material after various heat-treatments in the temperature range of 600 to 850℃.

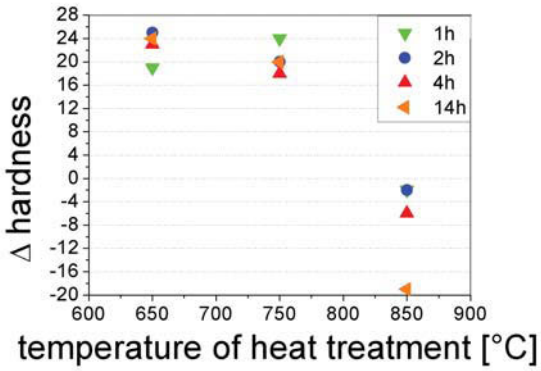

Fig. 4-13: Hardness change of VBS material after various heat-treatments in the temperature range of 650℃ to 850℃.

Based on the results of the Brinell hardness tests, heat-treatments for tensile test specimen were chosen.

4.3. Tensile tests

The most important results of tensile tests are discussed in this section. Additionally, the results of all tests are summarized in Appendix A.

4.3.6. Room temperature and 800℃ tests on LCS mate rial

The strengthening mechanisms for room temperature - except solid solution strengthening and precipitation hardening - are different, then those active at elevated temperatures [38]. Based on the results of the Brinell hardness measurements, the heat-treatments for the tensile tests of LCS material conducted at room temperature were chosen. The tensile properties of LCS material at room temperature were tested for three different annealing conditions. The results of Young's modulus (E), yield strength ($R_{p0.2}$) and tensile strength (R_m) are presented in Fig. 4-14. In addition to that, the tensile properties of LCS material as-extruded condition are given. The highest strength could be observed by short time annealing little below T_β followed by subsequent water quenching and an additional heat-treatment at 650℃ for 8h with air cooling. However , annealing only at 650℃ will increase $R_{p0.2}$ significant, but this temperature results in a lack of ductility. Various heat-treatments on LCS material were conducted at service temperature (800℃). The as-extruded state of LCS shows a tensile strength of 170 MPa, as shown in Fig. 4-15. The heat-treatments with satisfying room temperature properties could not be

related to high temperature applications, whereas annealing at 1010℃ for 20 minutes followed by 650℃ for 8 h resulted in the highest strength at room temperature. At elevated temperatures, however, the lowest values were observed. All heat-treatments performed at 800 and 850℃ have gained $R_{p0.2}$ values above 220 MPa, which was the target for the valve blanks. A heat-treatment at 850℃ for 8 h, then water quenched and additionally annealed for 8h at 650℃ and a heat-treatment at 800℃ for 24h achieved both a $R_{p0.2}$ of 226 MPa.

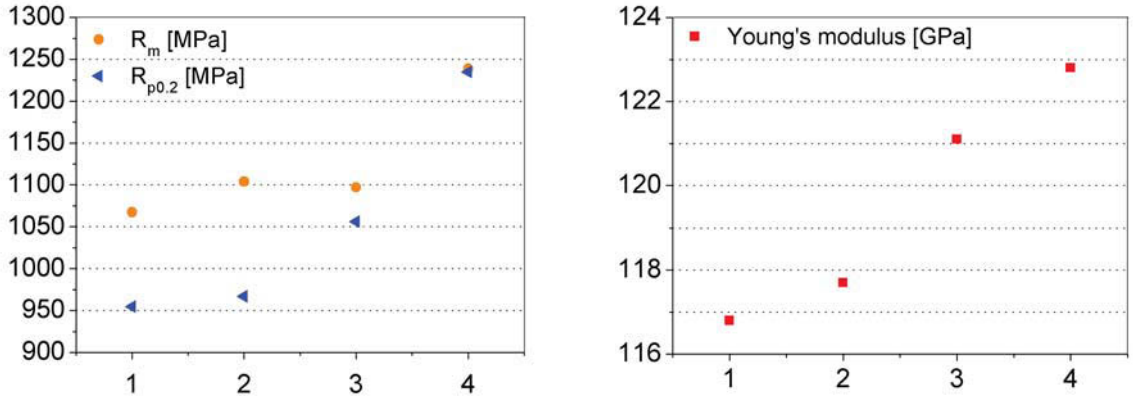

a) b)

Fig. 4-14: a) Tensile strength, yield strength and b) Young's modulus at room temperature for LCS material in starting condition (1) and after different heat treatments: (2) 850℃ 8h WQ, (3) 650℃ 8h AC and (4) 1010℃ 20 min WQ 650℃ AC.

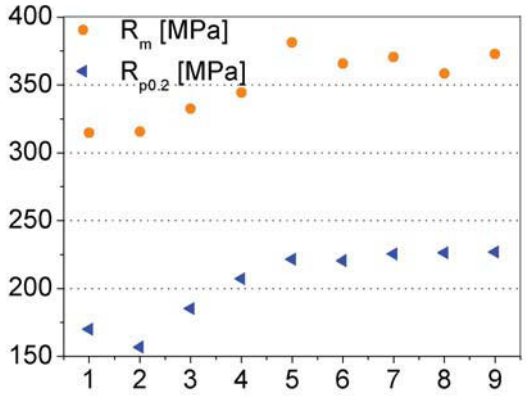

(1) as-extruded
(2) 1010℃ 20 min WQ 650℃ AC
(3) 650℃ 8h AC
(4) 800℃ 8h WQ
(5) 850℃ 8h AC
(6) 850℃ 8h AC 650℃ 8h AC
(7) 850℃ 8h WQ
(8) 800℃ 24h WQ
(9) 850℃ 8h WQ 650℃ 8h AC

Fig. 4-15: LCS tensile properties at 800℃ (service temperature) in starting condition (as-extruded state) and after different heat treatments.

4.3.7. Tensile tests at elevated temperatures on valve blanks

The starting condition promotes VBU as the most promising material, even better than LCS material. VBU exhibits with 184 MPa clearly the highest yield strength of the stem (see Fig. 4-16), whereas VBS and VBT suffered from processing from the LCS material to the valve blank, as shown in a lower yield strength compared to LCS material. VBT material shows the lowest starting condition with a yield strength of 148.5 MPa and was thus neglected.

Promising heat-treatments at 850℃ were performed o n the valve blanks. Fig. 4-17 displays a comparison of LCS, VBS and VBU in heat-treated conditions. However, only LCS material in an as-extruded state can exceed the goal of 220 MPa. VBU material shows the best properties of the valve blanks by reaching 195 MPa after annealing at 800℃ for 24 h followed by water quenc hing (VBU 2 state). From reference [39] it is tempting to speculate that the strengthening effect in NB4 at high temperatures is likely to be solid solution strengthening. This means that NB4 will not substitute IMI 834 and the design of a high intermetallic α_2-content and a suppressed β-phase were not as effective as assumed.

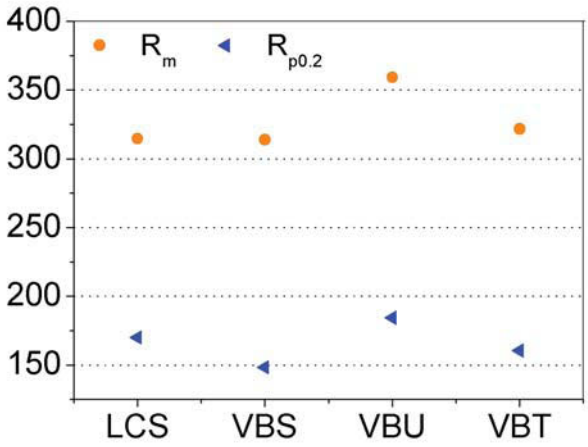

Fig. 4-16: Tensile strength R_m and yield strength $R_{p0.2}$ of LCS, VBS, VBU, and VBT starting material at 800℃.

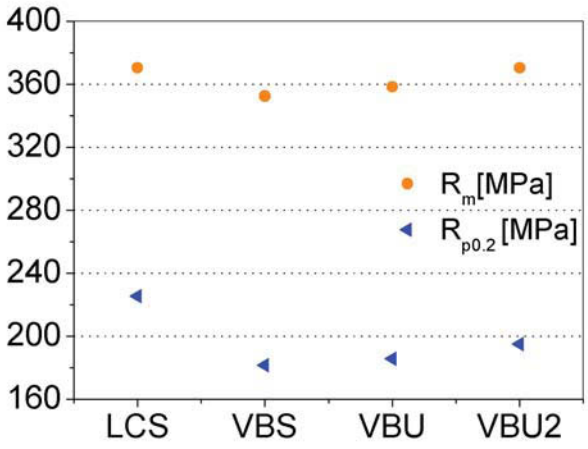

Fig. 4-17: Tensile properties of LCS, VBS, VBU at 800℃ after a heat-treatment at 850℃ for 8 h and followed by water quenching. Properties of VBU could be further improved by a heat-treatment at 800℃ for 24 h (VBU2 state)

VBU material heat-treated at 800℃ for 24 h and water quenched showed the best tensile properties at service temperature, but it was not high enough to succeed IMI 834. Nevertheless, additional tensile tests at 600°C showed the superiority of NB4 with a $R_{P0.2}$ of 575 MPa compared to 529 MPa of IMI 834 [17].

4.4. Analysis of the heat-treated microstructures

In order to understand the results of the tensile tests, the microstructures of the heat-treated LCS and VBS materials were investigated.

4.4.1. Microstructure of heat-treated LCS material

LCS material in the as-extruded state, as presented in chapter 4.1.1, showed equiaxed lamellar grains surrounded by a grain boundary phase. Fig. 4-18 shows the influence of different heat-treatment temperatures and, for 650℃, also the influence of time on the evolution of the microstructure. The change between 650℃ and 750℃ is barely seen in the light optical images of Fig. 4-18. At 750℃, the microstructure looks finer and the grain boundaries show a smoother morphology compared to the 650℃ variant. The influence of temperature is clearly seen at 850℃ by the dissolution of the lamellae and the grain boundary phase; bright lamellae are broadened and dark regions are fragmented. The contrast of microstructural appearance is lost and replaced by a more featureless look, where the original grain

boundaries are hard to detect. However, effects can not be detected. Long-time annealing did not show a distinctive influence on the microstructure.

The decrease of hardness and strength, tested at room temperature, from 650℃ to 850℃ discussed in chapters 4.2 and 4.3 can be explained by the observed dissolution of lamellar microstructure and the missing α-phase on the grain boundaries. However, tensile tests conducted at service temperature (800℃) presented a superiority of heat-treatments (see Fig. 4-15) performed at or above the service temperature followed by water quenching.

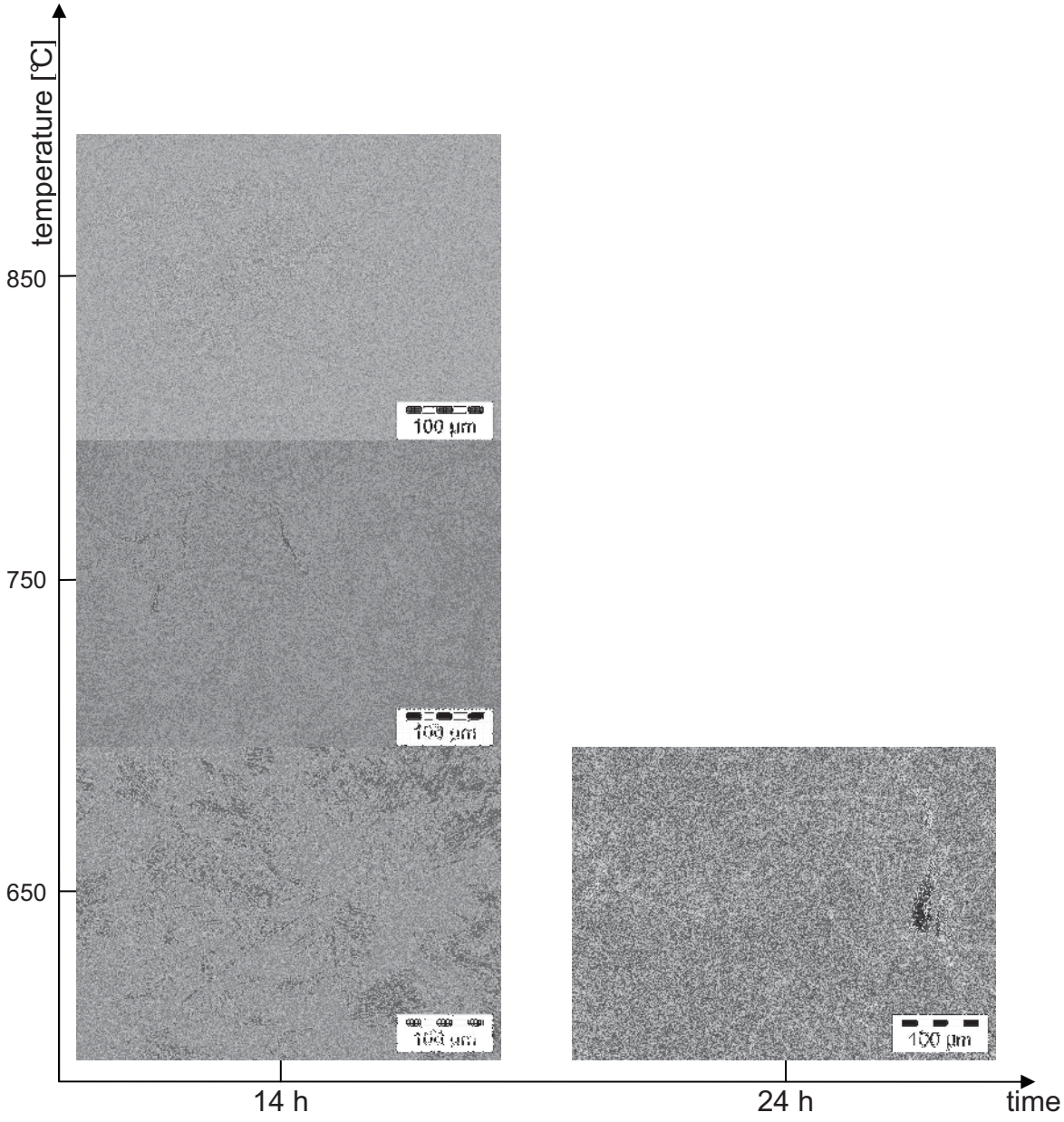

Fig. 4-18: Influence of heat-treatments on the microstructure of LCS material. With higher temperature, the lamellae broaden and appear fragmented (light optical images).

Fig. 4-19 shows the LCS material heat-treated at a) 650℃, b) 800℃ and c) 850℃ for 8 h on the left hand side and with an additional annealing at 800℃ for 8 h on the right hand side (d, e and f). The second treatment was conducted to investigate the influence of the service temperature on the annealed microstructure. As expected, the heat-treatment at 650℃ can not survive the add itional heat-treatment at 800℃ (d). Lamellae broadened slightly when the material was exposed twice the time to service temperature, as displayed in b) and e) of Fig. 4-19. Images c) and f) of the same figure do not present the same effect of 8 h at service temperatures for LCS material heat-treated at 850℃.

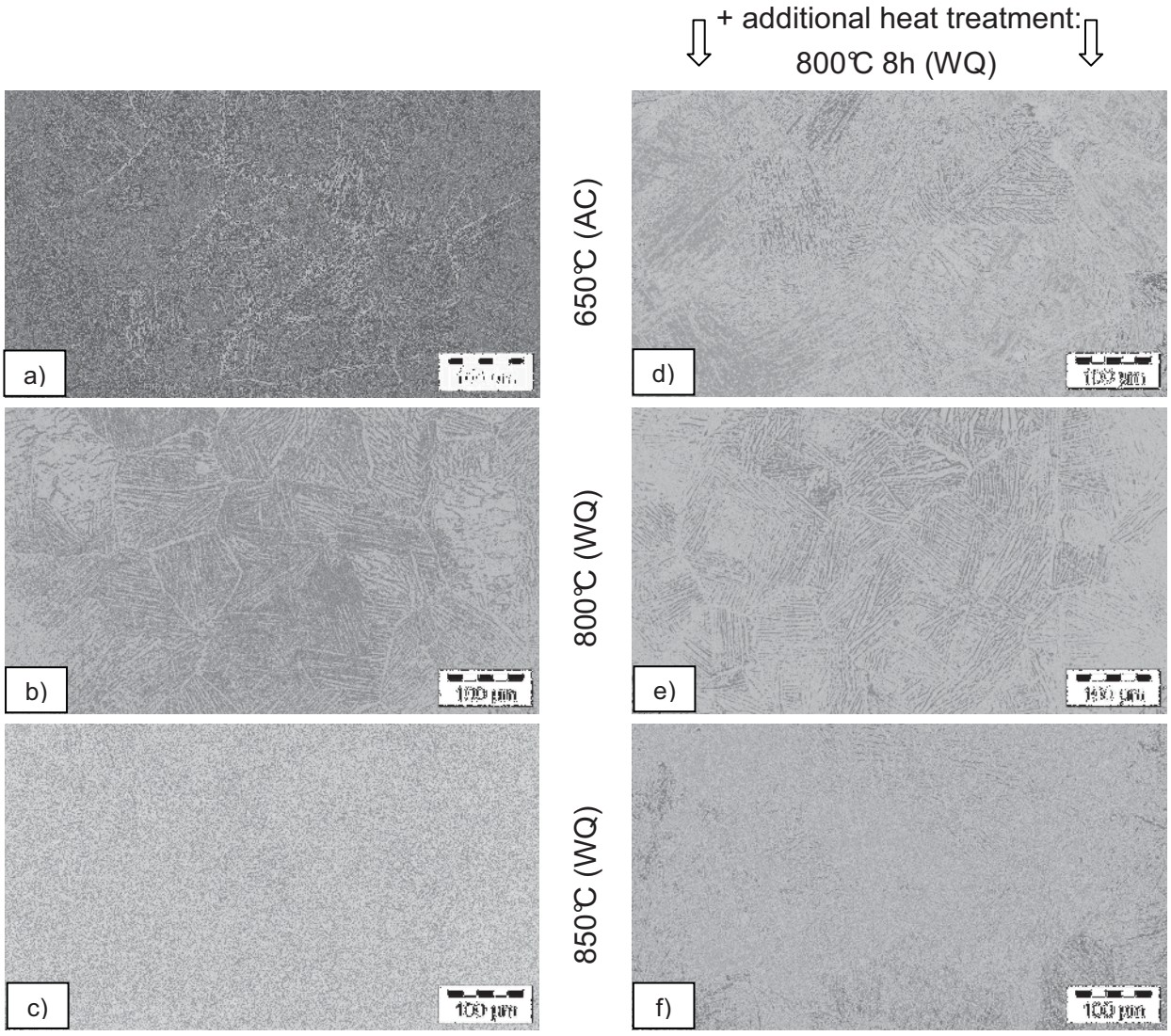

Fig. 4-19: Samples annealed at a) 650℃, b) 800℃ and c) 850℃ and additional heat-treated for 8h at 800℃ to simulate service conditions (d, e and f) (light optical images).

The influence of time on the microstructure of the LCS material annealed at 30℃ below T_β (1010℃) is presented in Fig. 4-20. This influence triggers a broadening of

the lamellae, though dissolution of the lamellae observed in case of 850℃ did not occur.

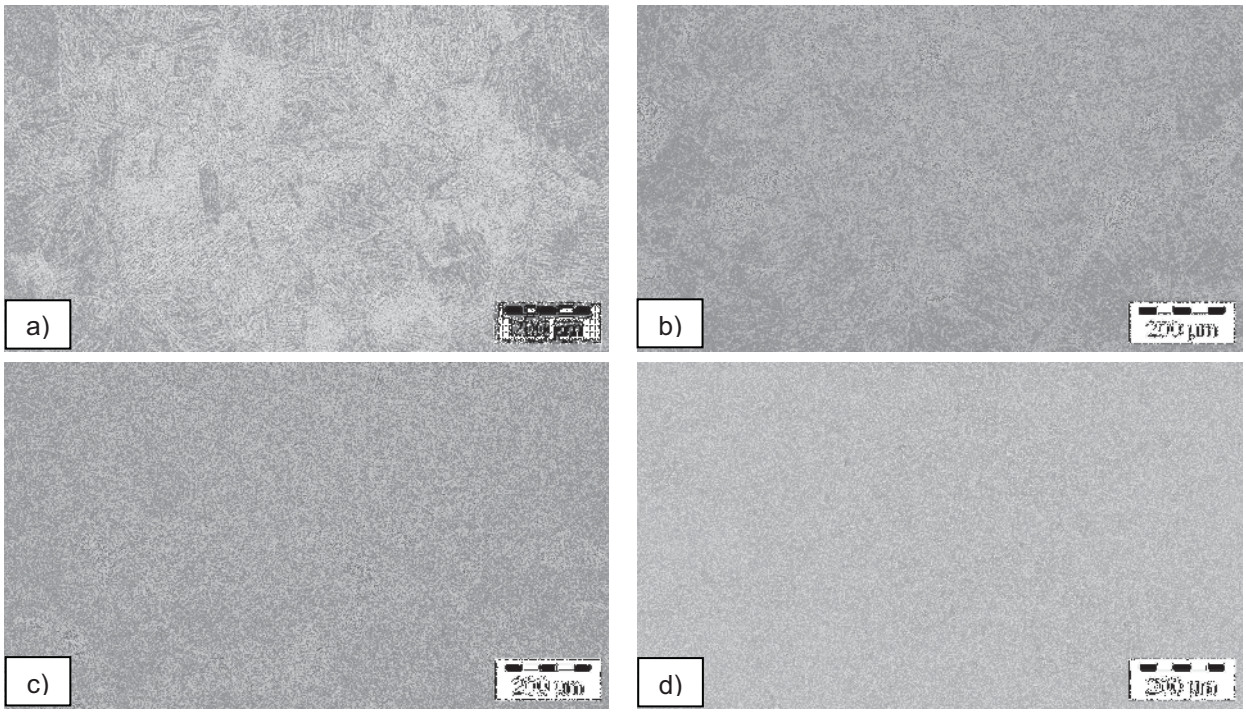

Fig. 4-20: Light optical images of LCS microstructures annealed at T_β-30 (1010℃) for a) 20 min, b) 30 min, c) 1 h, and d) 2 h.

4.4.2. Microstructures of heat-treated VBS material

By annealing at different temperatures, the VBS material presented in Fig. 4-21 shows similar effects as described in section 4.4.1 for LCS material. Again, at higher temperatures dissolution of the lamellae can be observed. However, this effect is not as tremendous as presented for LCS material in Fig. 4-20.

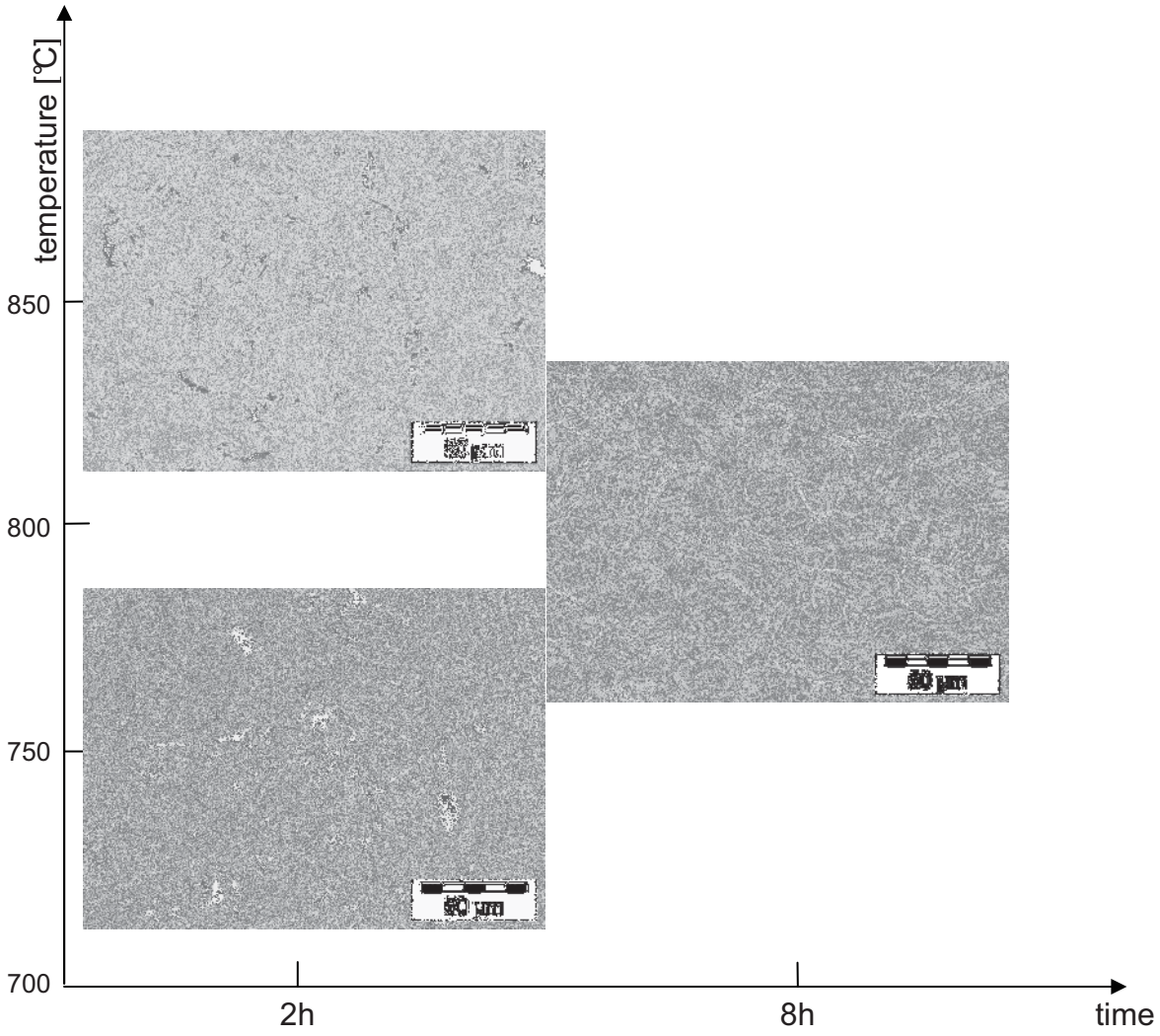

Fig. 4-21: Microstructures of VBS stem material, heat-treated at various temperatures and for different times (light optical images).

4.5. Dilatometry and deformation tests

The characterization of the deformation behavior and the influence of deformation rate and cooling condition on the microstructure were performed by means of deformation tests conducted in a dilatometer. As already mentioned in chapter 3.5, the temperature was controlled by two thermocouples that were fixed in the middle and on the edge of a cylindrical sample. The temperature curves of both thermocouples are shown in Fig. 4-22. Since no significant difference in the measured temperature was detected, the heat transfer at both ends of the sample had successfully been prevented by the Mo plates, which were connected to the sample using commercially available glue.

All samples elongated similar as shown for sample 1 (deformation speed = 100 mm/s, temperature = 1090℃) in Fig. 4-22. Curves of other conditions are presented in the Appendix B. At a temperature around 170℃, the increasing elongation curve is interrupted by a small peak indicating the evaporation of the super glue. T_β is reached at 1037℃, which indicates the phase transformation from α-Ti into β-Ti. After holding at maximum temperature, the start of deformation can be seen in an immediate decrease of the samples height (arrow in Fig. 4-22). The according load and true stress curves of the deformation process are shown in Fig. 4-23.

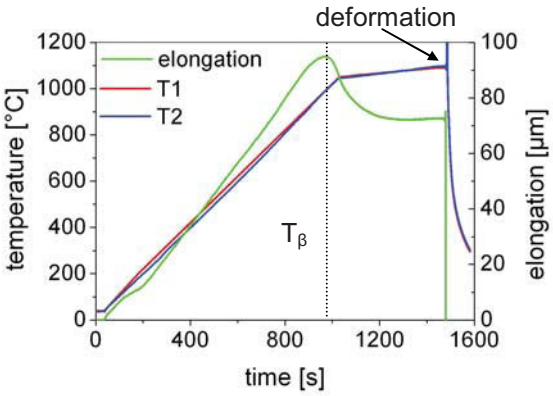

Fig. 4-22: Course of temperature and deformation during the deformation test of sample 1. T1 and T2: temperature of thermo-couple 1 and 2.

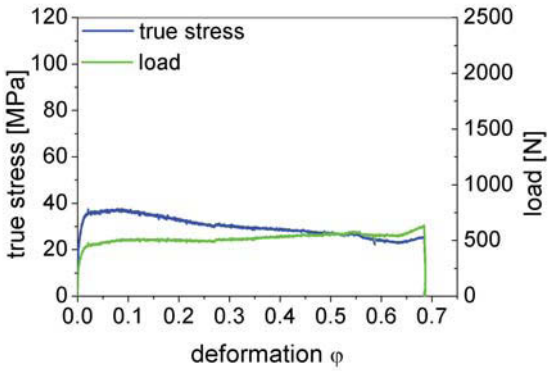

Fig. 4-23: True stress / load deformation curves as recorded for sample 1.

Fig. 4-24 compares the obtained load (a) and true stress (b) curves of samples deformed with three different deformation speeds at 1090℃. The highest load and true stress can be measured for the highest deformation speed. The lower the deformation rate is, the lower is the load and the corresponding true stress.

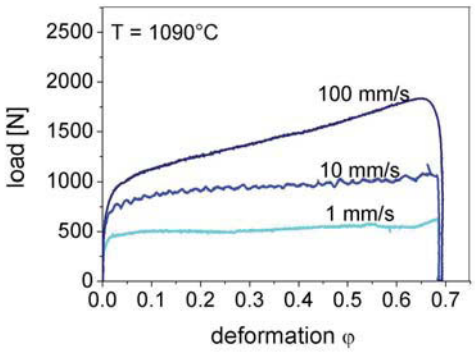

a)

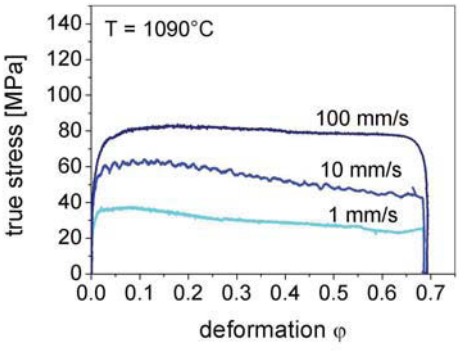

b)

Fig. 4-24: Comparison of deformation curves as a function of a) load and deformation rate and b) true stress and deformation rate at 1090℃. Deformation followed by subsequent water cooling.

Fig. 4-25 shows the influence of different deformation temperatures on the applied load and the measured true stress, while the deformation speed stays constant. The higher the temperature is, the lower is the applied load and the corresponding true stress. However, low temperatures implement high loads and high true stress.

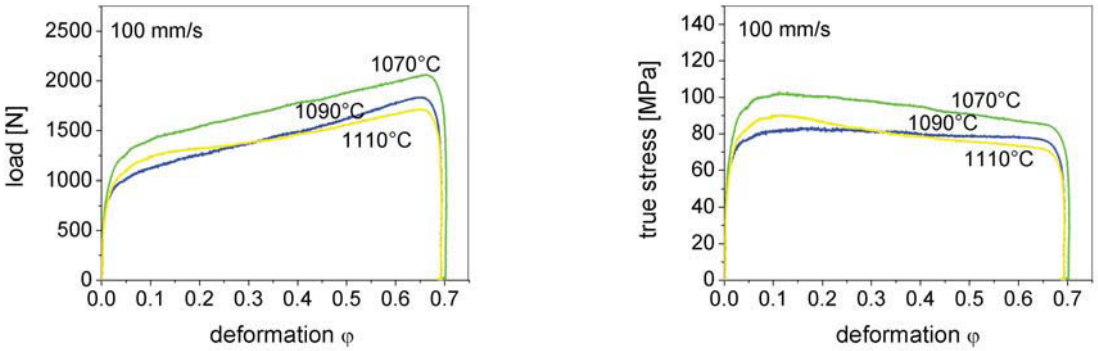

a) b)

Fig. 4-25: Comparison of deformation curves as a function of a) load and deformation temperature and b) true stress and deformation temperature and a constant deformation speed of 100 mm/s. Deformation followed by subsequent water cooling.

Up to now, only deformation curves of the first cooling condition (subsequent water cooling (WQ)) were presented, since cooling does not influence the deformation. Fig. 4-26 shows the correspondence of the two deformation curves as a function of load on an arbitrarily sample. Difference refer to typical experimental variations

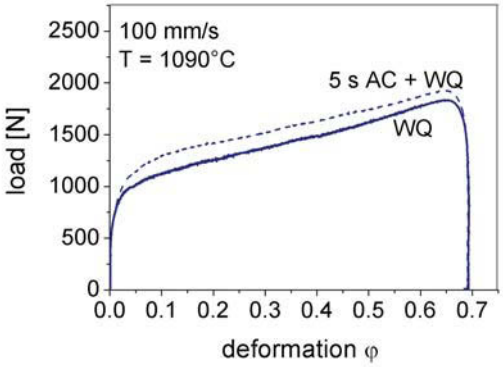

Fig. 4-26: Comparison of an arbitrary deformation curve depending on the cooling condition.

After deformation, the samples show a symmetrical barrel-like appearance, as shown in Fig. 4-27, and the surface appeared to be considerably rough, as shown in Fig. 4-28 for sample 1.

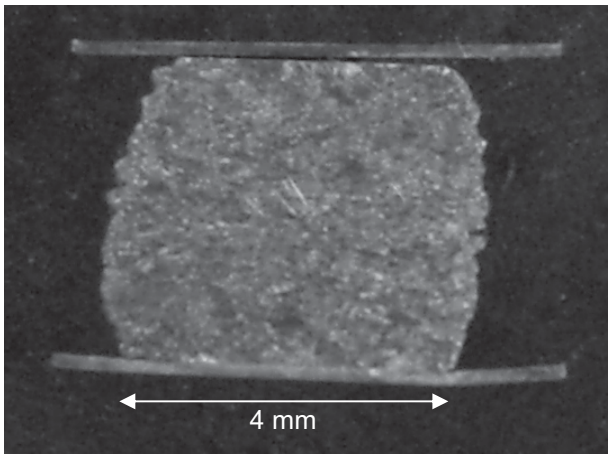

Fig. 4-27: Dilatometer sample after reduction to 50% of its height.

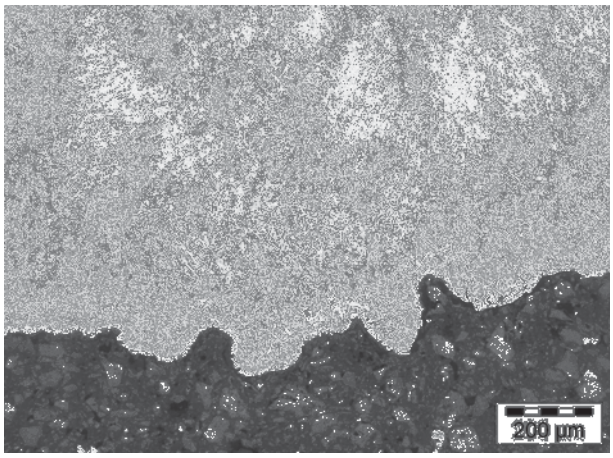

Fig. 4-28: Surface of a dilatometer sample after deformation.

The starting microstructure for these investigations was described in 4.1.1 (LCS material). The maximum grain size of the equiaxed grains was about 250 µm.
For all settings, different microstructures were achieved and summarized in Fig. 4-29 and Fig. 4-30.
Depending on the settings of the deformation process, the microstructure partly stayed initially and deformed, and partly shows dynamically recrystallized features. The deformed grains showed a pancake-like appearance. The results indicated a dependency on the deformation speed. With increasing deformation speed, the grains are more elongated. This trend was specifically determined in the first run (WQ), but was not achieved in the second (5 s AC and WQ).
Higher deformation temperatures result in larger deformed grains, which leads to the assumption that the grains grew before and after deformation. At a deformation temperature of 1110℃, the grains started growing e normously and thus led to a decreased fraction of dynamically recrystallized areas.
Both deformation settings showed principally the same tendency. The influence of the air cooling step before the actual water cooling can be seen when achieved microstructures are compared. The second variant showed decreased grain growth and wide areas of recrystallized microstructure. The optimum microstructure, i.e. a fully dynamically recrystallized microstructure, can be obtained when the material is deformed at the lowest temperature and the highest deformation speed.

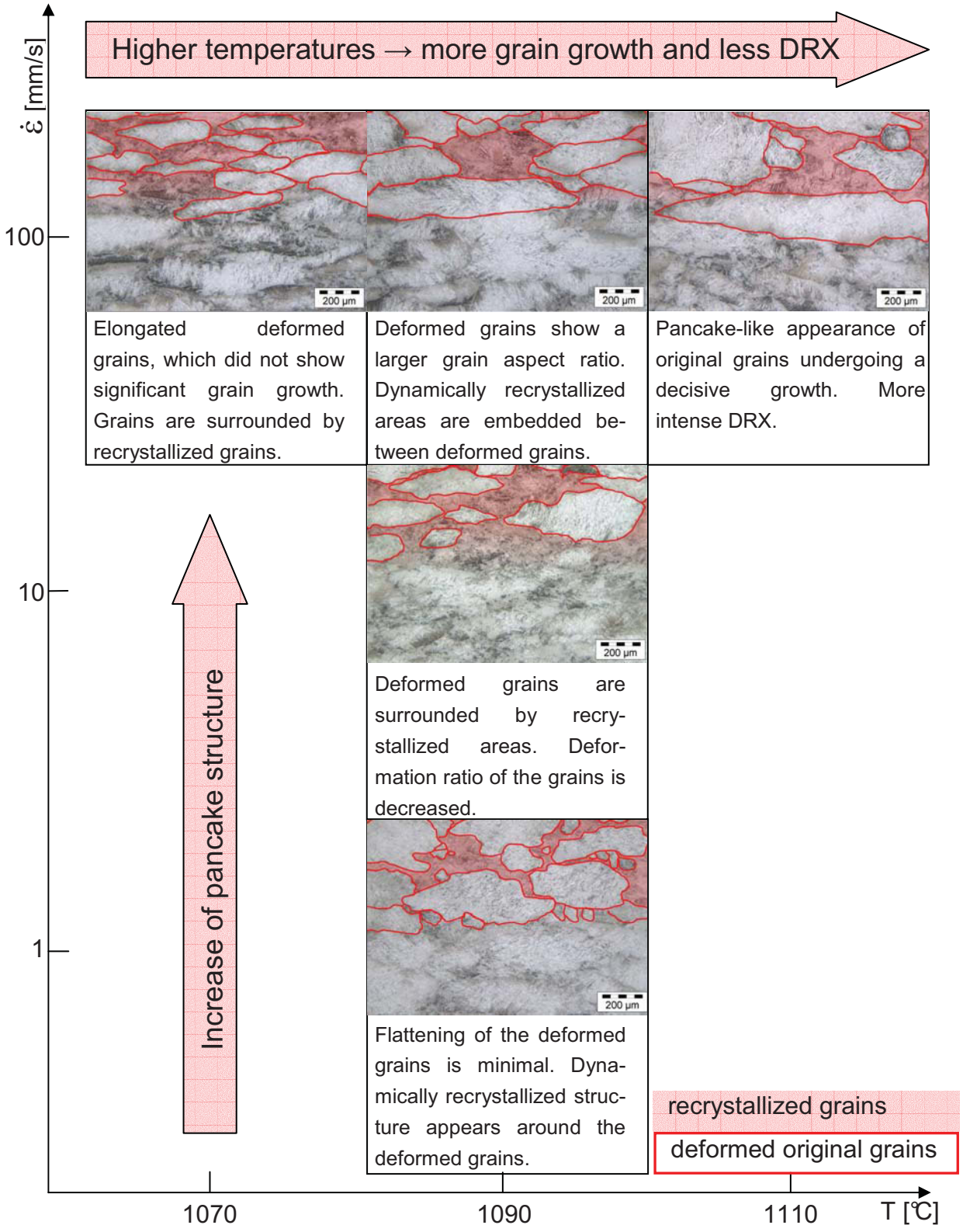

Fig. 4-29: Evolution of the microstructure during deformation at different rates and temperatures. Subsequent to deformation the samples were water quenched.

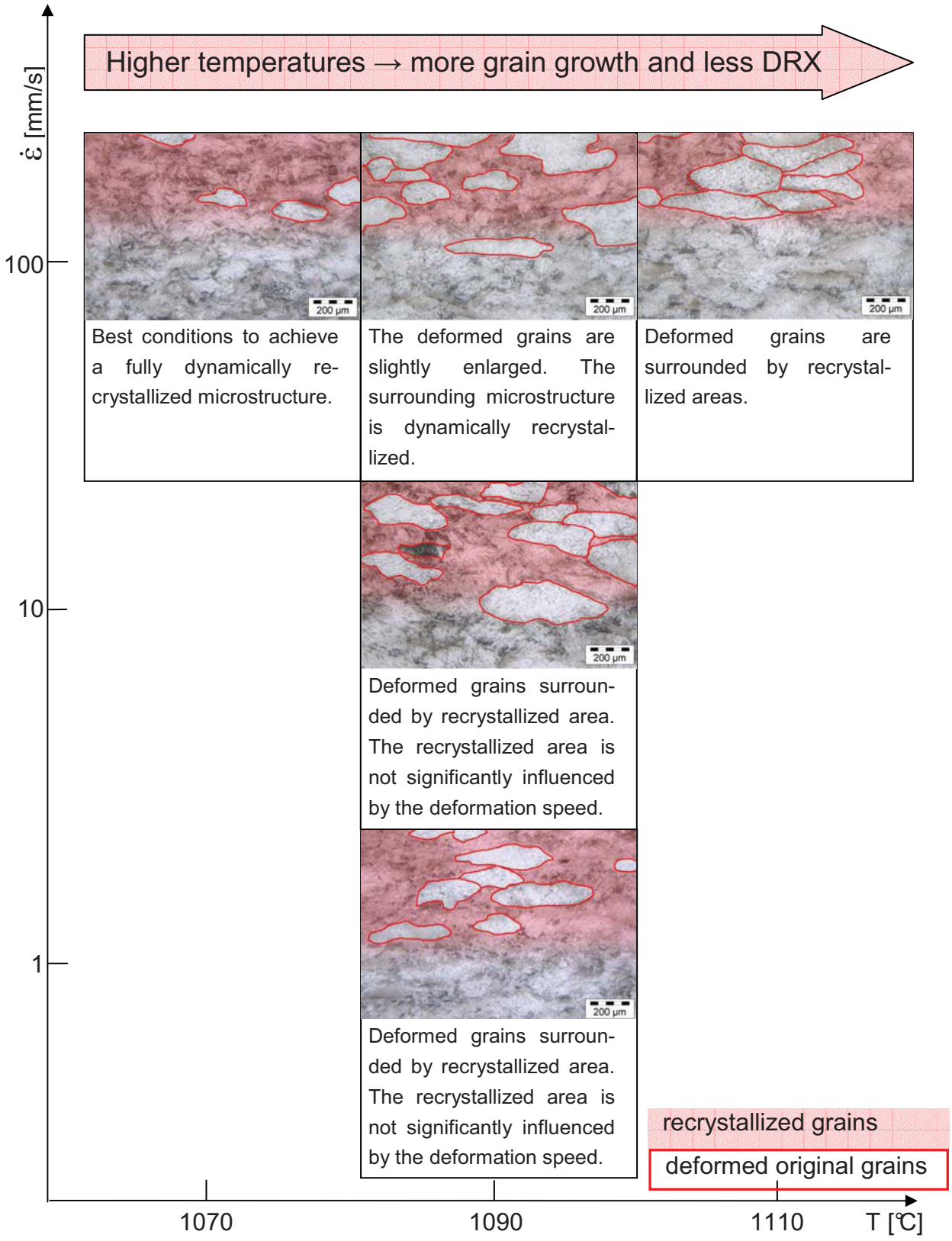

Fig. 4-30: Evolution of the microstructure during deformation at different rates and temperatures. Samples were cooled by subsequent air cooling for 5 seconds and water cooling afterwards.

4.6. Phase analysis

Thermodynamic calculations predicted the existence of 40-50 vol.% α_2 as shown in Fig. 3-1. The aim of the phase analysis was to prove the α_2-phase and to determine the existing volume fraction of α_2. Interest was laid upon two heat-treated states of VBS material (14 h 650℃ followed by air cooling and 8 h 800℃ subsequently water quenched). The second condition was of higher interest, since results of the tensile tests revealed the benefit of this heat-treatment. Corresponding microstructures were already displayed in chapter 4.4.2.

4.6.3. Quantitative phase analysis

Equiaxed grains of the acicular microstructure, represented by light and dark lamellae, are surrounded by a light grain boundary phase, as shown for both tested states in Fig. 4-31 (650℃) and in Fig. 4-32 (800℃). The following evaluation was based on the assumption that α corresponds to the bright and α_2 to the dark areas.
The classification into dark (α_2) and bright areas (α) gave a ratio of about 50:50 vol.% for the heat-treatment conducted at 650℃ and 40:60 for the heat-treatment performed at 850℃, the later percentage representing the fraction of α-phase (see Tab. 4-1)

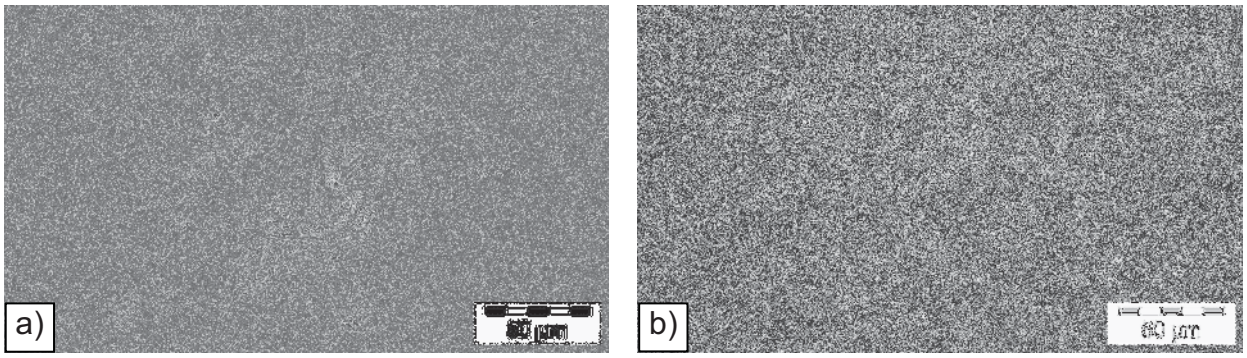

Fig. 4-31: Microstructure of VBS material heat-treated at 650℃ for 14h. a) Light optical image; b) same image as a), but the contrast was enhanced by using the software ANALYSIS.

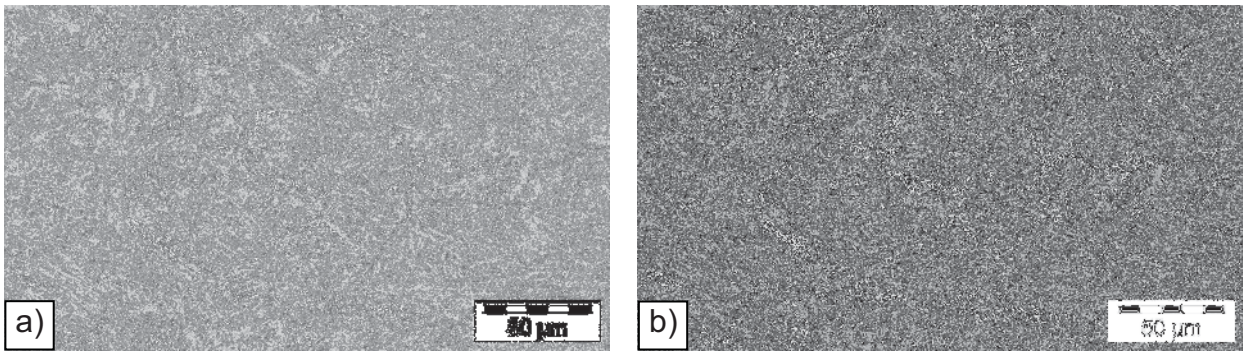

Fig. 4-32: Microstructure of VBS material heat-treated at 800℃ for 8h. a) Light optical image; b) same image as a), but the contrast was enhanced by using the software ANALYSIS.

Tab. 4-1: Results of the quantitative phase analysis of two different states of VBS.

HT	α [vol.%]	α_2 [vol.%]
650℃ 14 h AC	53	47
800℃ 8h WQ	60	40

This first attempt of quantifying the microstructure comprises a number of possible errors, since dark and light areas vary just slightly in contrast and might not be distinguished properly over the whole image. This is even more pronounced for the material heat treated at 800℃.

4.6.4. XRD

Since α_2 is the ordered phase of α, XRD-peaks are close together. However, peaks at low angles, representing low indicated planes, clearly proof the presence of α_2 as shown in Fig. 4-33 for the sample annealed at 650℃ . For the second sample, those peaks were not achieved, but the broadness of the detected maxima is a sign for two overlapping peaks. A possible reason for not detecting the low indexed peaks could be the rather low intensity of the spectrum.

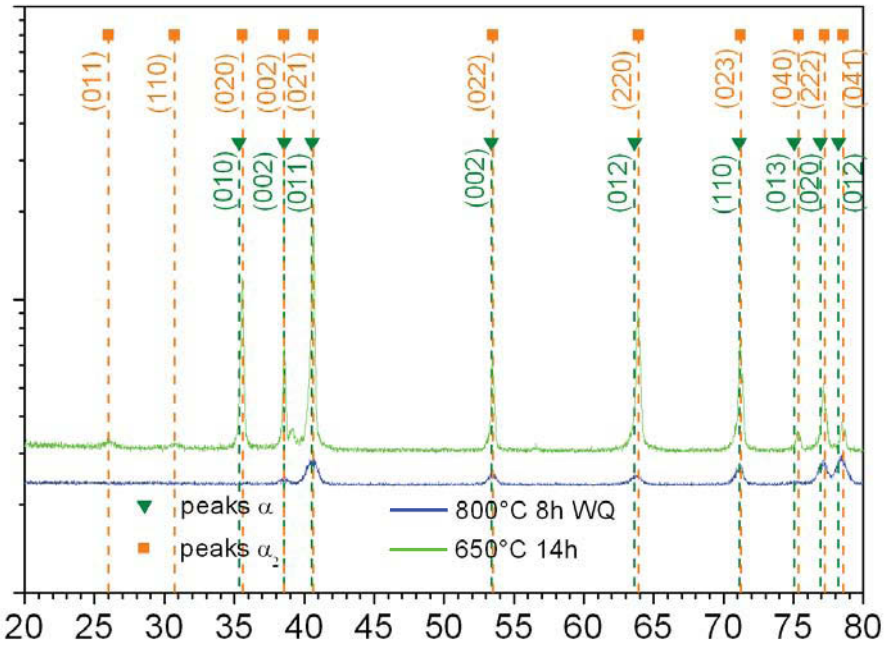

Fig. 4-33: XRD spectra of VBS material in two different heat-treatment states. The position of the α- and α_2-reflexes are indicated.

The tool of Rietveld analysis, which describes the XRD spectra by analytic functions, revealed the percentage of measured α and α_2 for both settings as presented in Tab. 4-2. To confirm the concurrent existence of the phases α and α_2, Rietveld analyses were additionally done by assuming a non-existence of α. This fictitious assumption showed a mismatch of the calculated spectra according to the Rietveld method with the measured spectra and confirmed the existence of α_2. The method also offered the possibility to calculate the fraction of β, which proved to be very limited. However, the results comply with those of quantitative phase analysis.

Tab. 4-2: Volume fractions of α-, α_2- and β-phases of two different states of VBS as determined by Rietveld analysis.

HT	α [vol.%]	α_2 [vol.%]	β [vol.%]
650℃ 14 h AC	62	35	3
800℃ 8h WQ	54	45	1

The tested samples were originally machined from the stem. A highly textured and deformed region results in a loss of accuracy of the XRD measurements, thus an inexact Rietveld evaluation can be expected. Due to the difficulties to separate the ordered and unordered reflections, a higher inaccuracy has to be accepted. The

correctness of the results given in Tab. 4-2 can be assumed to be in the range of +/- 5 %.

4.6.5. EBSD

Based on electron back scattered diffraction (EBSD) characterization and quantification of each phase fraction (α, α_2 and β) were conducted. The pattern quality maps shown in Fig. 4-34 and Fig. 4-35 display the acicular microstructure of the materials. Yellow pixels represent detected α-Ti, magenta α_2-Ti_3Al and red the very limited β-phase. The examined section of the first sample (650℃ 14h AC) was too small to give a representative overview of the microstructure. This might be the reason for the controversial result obtained for the α/α_2-volume fraction as presented in Tab. 4-3. Since Rietveld analysis leads to a ratio of about 50:50 vol.% of α and α_2 (see Tab. 4-2), and also the phase calculation basically predicts a higher α-content (see Fig. 3-1) , the result will not be considered in the further discussion.
The results of the analysis of the second sample continue the trend and leads to a ratio of about 50:50 for the present α and α_2-phases. As displayed in Fig. 4-35, α_2 forms lamellae and is also distributed in the α-phase. The percentage of β is marginal and the phase was basically detected on phase boundaries.

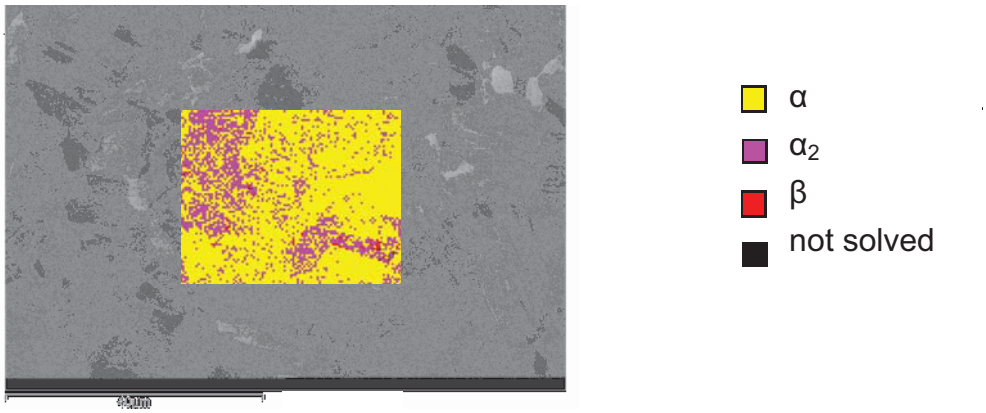

Fig. 4-34: Pattern quality map and a partial phase map of VBS material annealed for 14h at 650℃.

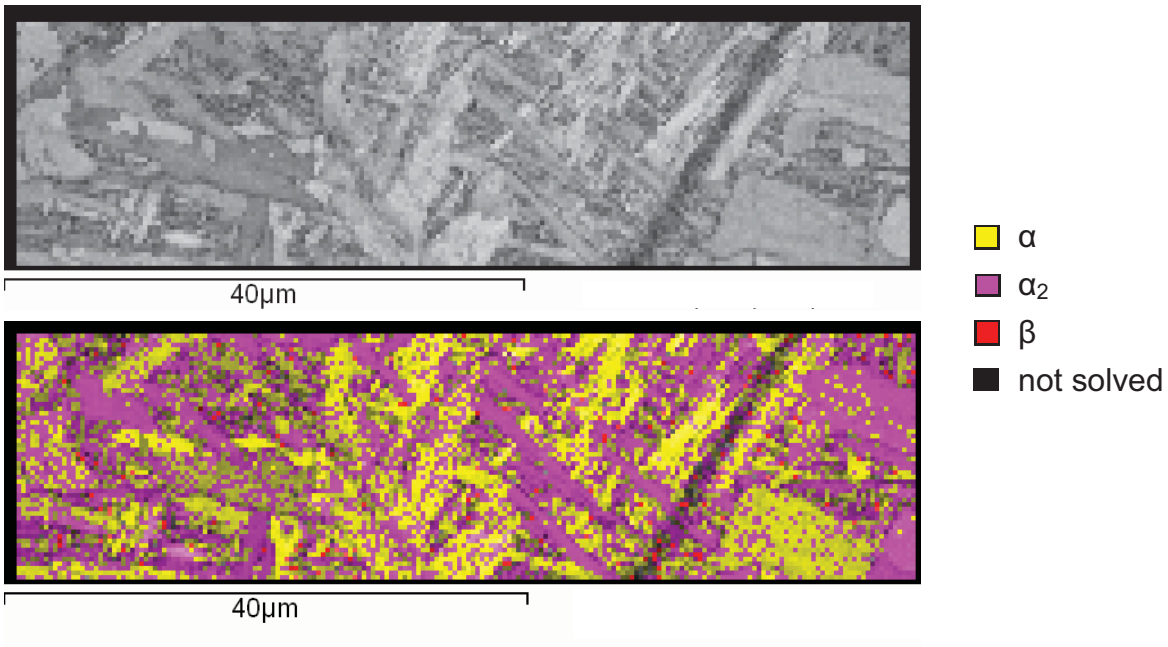

Fig. 4-35: Pattern quality map (PQM) and PQM overlaid with the phase map of VBS material heat-treated for 8h at 800℃.

Tab. 4-3: Results of the phase analysis by using EBSD of two different states of VBS.

HT	α [vol.%]	α_2 [vol.%]	β [vol.%]
650℃ 14 h AC	26	73	1
800℃ 8 h WQ	56	43	1

EBSD revealed nearly the same difficulties and sources of errors as XRD. The similarity of the α and the ordered α_2-phase as well as the texture of the material bear an inaccuracy of results of about +/- 5 %. The rather small analyzed area of approximately 20x80 µm² permits only a low statistic of the examined microstructure. Long measuring time did not allow for analyzing larger areas. During performing a high resolution scan on the second sample (Fig. 4-35), a rapid contamination of the sample with atomic carbon was detected, which limits this method for closer investigations.

4.6.6. Comparison of results

A comparison of the results for both states is shown in Fig. 4-36. Only the EBSD measurements of VBS material annealed at 650℃ must be excluded based on reasons stated in the previous sections.

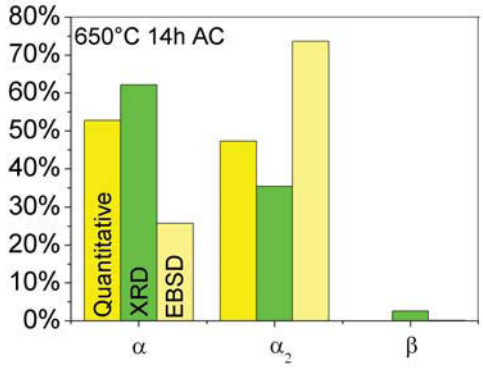

a)

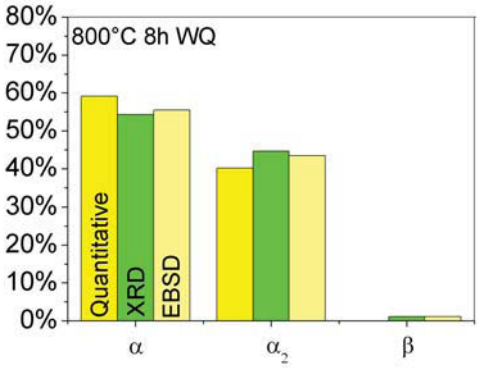

a)

Fig. 4-36: Comparison of the resulting phase fractions α, α_2 and β obtained by quantitative phase analysis, XRD and EBSD for a sample a) heat treated at 650℃ for 14h and air cooled and b) heat treated at 800℃ for 8h and water quenched.

4.6.7. TEM

TEM investigations were firstly made to prove the presence of α- and α_2-phase and secondly to show that the lamellar microstructure is represented by alternating α- and α_2-lamellae. Since the microstructure was similar for both setups (650℃ 14 h AC and 800℃ 8 h WQ), the investigations were limited to V BS material, which was annealed at 800℃. The ordered α_2-phase, well displayed for region 5 of Fig. 4-37, can be distinguished by the presence of forbidden diffraction patterns, that are typical for ordered crystal systems.

The sequence 1-4 in the upper image of Fig. 4-37 proves the lamellar arrangement of the phases α and α_2. However, this lamellar structure was not observed for region 5-7 (lower image of Fig. 4-37).

For full characterization of the arrangement of phases, further and more extensive TEM investigations are recommended.

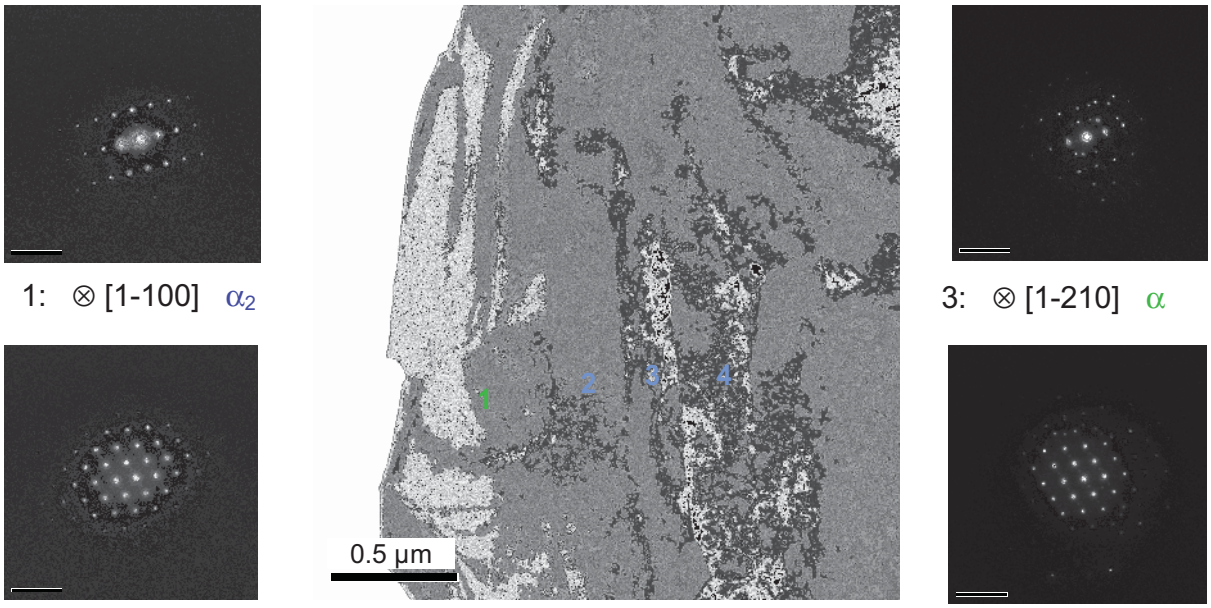

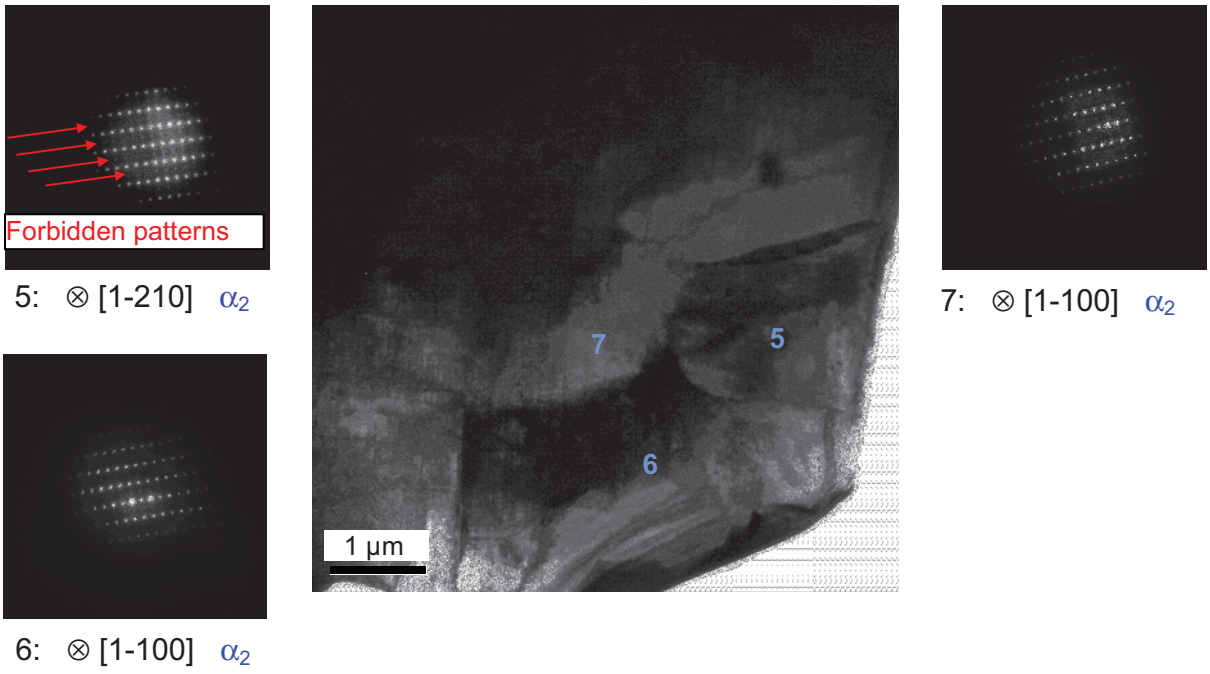

Fig. 4-37: Region investigated by TEM and the corresponding diffraction patterns of the detected phases (VBS material annealed at 800℃ for 8h, wate r quenched).

4.7. Oxidation

Samples of NB4 (VBS, VBT, VBU), NB7, Alloy 2 and IMI 834 were taken from the valve head area to test the oxidation resistance. All alloys showed a parabolic oxidation behavior as predicted for near-α-titanium alloys [27]. The weight gain curve of IMI 834 matches well with the results reported by M. Peters et al. [18] (see Fig. 2-18). The comparison of the three NB4 versions shows, that after 24 h the difference of weight gain was 0.8 mg/cm² between the VBS, the NB4 version with the highest increase in weight, and VBT the version of lowest increase. This difference is significantly high, since NB4 materials did not differ in chemical composition and only showed differences in microstructures. The microstructures of the starting materials are additionally displayed in Fig. 4-38. VBS, VBU, Alloy 2 and NB7 have a similar microstructure. The main difference between the individual NB4 microstructure is the larger grain size of the VBT condition. The weight gain curve of Alloy 2 showed the second highest increase of weight. Best oxidation resistance is obtained for NB7, which was expected since this alloy has the highest Nb content. Niobium is an element known to promote the oxidation resistance of Ti-alloys [26].

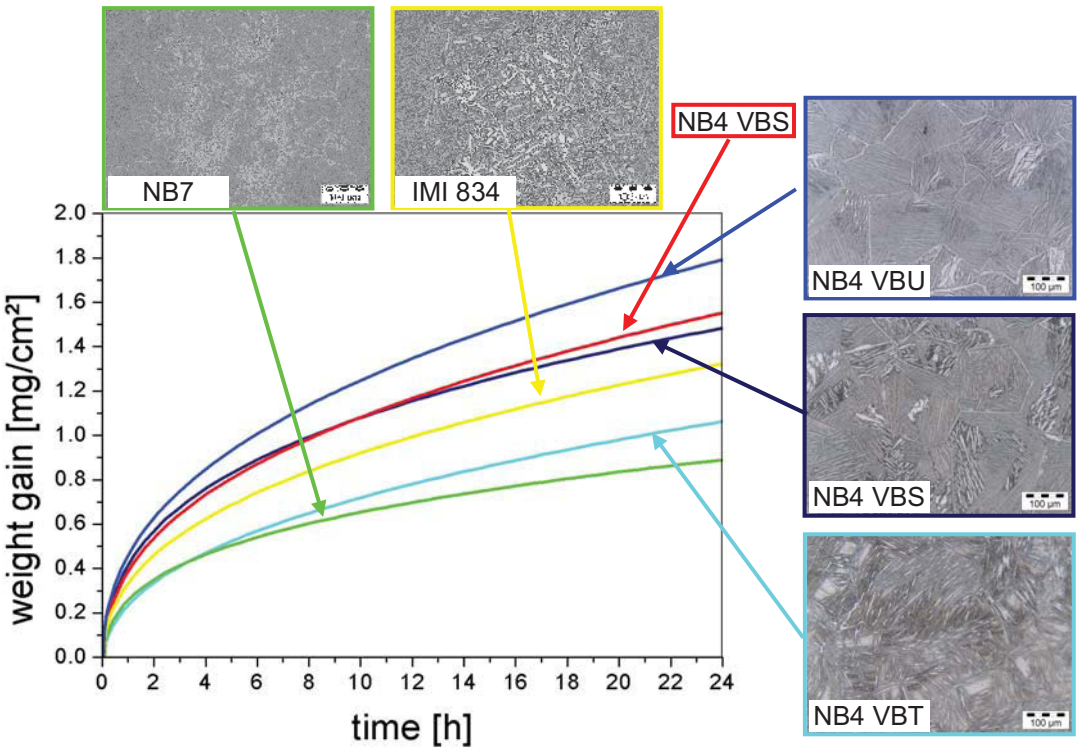

Fig. 4-38: Weight gain as a function of oxidation time for different near-α-alloys (static oxidation test in air). In addition, images of the representing microstructures are displayed.

5. Summary and conclusions

The company DaimlerChrysler AG in collaboration with the Department of Physical Metallurgy and Materials Testing of the University of Leoben, has developed a new near-α-alloy to substitute the alloy IMI 834 as high-temperature material for valves to be used in competitive high perfomance engines. These valves have to endure temperatures up to 800℃ for 8 to 10 hours. As a de mand the volume fraction of intermetallic phases was restricted to 50 vol.%. Therefore, alloying elements were chosen to create a novel near-α-alloy that exhibits α_2-volume fraction close to 50 % and which shows only an insignificant amount of weakening β-phase. Thermo-dynamical calculations based on MatCalc were conducted in order to predict the appearing phases and their dependence on temperature.

The goal of this diploma thesis was to characterize this new alloy NB4 and to prove if the mechanical properties meet the desired requirements, for example, a yield strength ($R_{P0.2}$) above 220 MPa at a service temperature of 800℃.

The tested material was present in four different states, corresponding to the manufacturing process of the valves. The first state is the LCS condition, which is an extruded one. The other three states, VBS, VBU and VBT already present valve blanks that were forged and heat treated at different temperatures. VBS was forged 30℃ above T_β, whereas the forging process of VBU and VBT took place 30℃ below T_β. After the forging process, VBT received an additional heat treatment 30℃ above T_β. On these different states of the NB4 material, the characterization of the alloy was accomplished by various methods and techniques.

Since the exposure to service temperature also claims for satisfying oxidation resistance, corresponding oxidation tests were conducted at 800℃ for 24 h in air. Samples of VBS, VBU and VBT were compared with other near-α-alloys developed by DaimlerChrysler AG and the conventional near-α-alloy IMI 834. All alloys showed an parabolic oxidation behavior. The VBT condition has shown the best performance, whereas the VBU sample possessed the highest weight gain. This is probebly due to the larger grain size.

Another part of the investigation was the characterization of the deformation and dynamic recrystallization behavior of LCS material in order to simulate the processing of the valve blanks. This was done by deformation dilatometer tests, which differed in deformation speed and temperature. With increasing deformation speed or decreasing temperatures, higher true flow stresses were measured. After the

deformation step, two different cooling scenarios were conducted which had a significant influence on the microstructure. Low deformation temperatures increase dynamic recrystallization and thus decreased the volume fraction of deformed grains. A nearly fully recrystallized microstructure is obtained with the combination of lowest temperature (1070℃) and highest deformation speed (100 mm/s).

Equiaxed grains with a lamellar microstructure and a grain size of about 200 µm in the center of the extruded rod were presented in the microstructure of LCS material. Further, a grain boundary phase was observed to surround the grains and unrecrystallized areas, which are typical for extruded materials.

The examination of the microstructure of VBS material showed different microstructures within the head due to varying deformation grades and a homogenously and highly deformed stem, which exhibits a microstructure of equiaxed grains of a mean size below 20 µm. The microstructure achieved for the VBU condition is very similar to the one of the VBS state, though the grains of the stem have a mean size of about 10 µm. Because of the additional heat-treatment of VBT above $T_{ß}$ the microstructure looses the typical lamellar appearance and the continuous grain boundary phase splits up. The lamellar microstructure is replaced by a less ordered structure that is intersected by broad needles. The grains of the stem start with a grain size of 100 µm and increase up to 500 µm.

The first adjustment of the optimum microstructure was accomplished by heat-treatments on LCS and VBS material and verified by hardness measurements. The change in Brinell hardness varied in response to the heat-treatments, which differed in time and temperature. Both LCS and VBS materials showed the highest increase in hardness after a heat-treatment at 650℃. With h igher annealing temperatures, the benefit of the heat-treatment decreased and as for VBS material, a decrease in hardness after annealing at 850℃ was observed. The microstructure of the material which was annealed at 850℃ changed significantly, indicated by the dissolution both of lamellae and grain boundary structure within the original LCS and VBS microstructure. The observed decrease of hardness when the heat-treatment temperature is raised from 650℃ to 850℃ can be ex plained by the loss of the lamellar microstructure and the missing grain boundary phase.

Metallographic investigations on LCS material showed the influence of exposure to service temperature on differently heat-treated microstructures. A microstructure achieved from a heat-treatment at 650℃ as well as 850℃ changes to a microstructure, which is expected for a heat-treatment conducted at 800℃ (service temperature).

One of the alloy requirements, as mentioned above, was the restriction of the intermetallic α_2-phase to a maximum of 50 vol.%. Two interesting conditions of VBS material were tested, one annealed at 650℃ for 14 h and another heat-treated at

800℃ for 8 h. Quantitative phase analysis, XRD, EB SD showed an ratio of α and α_2 of about of 50:50, which agrees to thermo-dynamical calculations. Further, TEM investigation revealed the existence of α and α_2 and their lamellar arrangement.
Finally, tensile tests at room temperature and service temperature (800℃) on heat-treated LCS and valve blanks material were conducted. Based on the results of Brinell hardness, the heat-treatments were chosen for LCS and VBS material. The corresponding results confirmed the trends obtained by hardness tests and verified the strengthening effect of the heat-treatment conducted at 650℃.
Tensile tests at elevated temperatures were based on the aim to exceed a yield strength of 220 MPa, the critical value required for application. Heat-treatments started on LCS material in order to transfer the results to the valve blanks. The as-extruded condition of LCS material showed a yield strength of 170 MPa. A heat-treatment at 850℃ for 8h followed by water quenchi ng and an additional annealing step for 8 h at 650℃ as well as a heat-treatment a t 800℃ for 24 h achieved both a 0.2%-yield strength of 226 MPa. For the valve blanks, the starting situation promoted VBU as the most promising material, by reaching a yield strength of 184 MPa, which means that the forming process from LCS to the valve blanks is a beneficial effect, whereas VBS and VBT suffered during the transformation step. VBT material showed the lowest yield strength of 148.5 MPa and, therefore, was not considered for further investigations. After a heat-treatment at 800℃ for 24 h, VBU material displayed best tensile properties of the valve blanks by reaching a yield strength of 195 MPa. Therefore, tensile tests show a superiority of heat-treatments, which are conducted at or above the service temperature (800℃) combined w ith subsequent water quenching. These annealing procedures lead to the dissolution of the lamellas and the grain boundary phase as stated above. However, the goal of 220 MPa could not be reached and a substitution of IMI 834 will be difficult if not fatigue properties will show a benefit. Concerning static properties the design of a near-α-alloy with a high α_2 content and a suppressed β-phase was not as effective as assumed. However, additional tensile tests at 600℃ showed the superi ority of NB4 with a $R_{P0.2}$ of 575 MPa, compared to 529 MPa of IMI 834 [17]. Since the strengthening through the intermetallic α_2-phase was not sufficient, solid solution strengthening and particle strengthening could be advantageous, if a further development of this new class of high-temperature near-α-titanium alloys is considered.

References

1 P. Wanjara, M. Jahazi, H. Monajati, S. Yue, “Influence of thermomechanical processing on microstructural evolution in near-α alloy IMI 834”, Materials Science and Engineering A 416, 2006, p. 300-311

2 M. Peters, J. Hemptenmacher, J. Kumpfert, C. Leyens, “Structure and properties of titanium and titanium alloys” in “Titanium and titanium alloys” (ed. M. Peters, C. Leyens), Wiley-Vch-Verlag, Weinheim, 2003, p. 1-36

3 H. Kestler, H. Clemens, ”Production, processing and application of γ(TiAl)-based alloys“ in “Titanium and titanium alloys” (ed. M. Peters, C. Leyens), Wile-Vch-Verlag, Weinheim, 2003, p. 187-230

4 J. B. Newkirk, A. H. Geisler, Acta. Met. 1, 1953, p. 370

5 G. Lütjering, J. C. Williams, “Titanium”, Springer, 2003

6 C.R. Brooks, “Heat treatment, structure and properties of nonferrous alloys”, ASM 1982, chapter 9

7 S. Lampman, “Wrought titanium and titanium alloys” in “ASM Handbook Volume 2 – Properties and selection: Nonferrous alloys and special-purpose materials”, ASM International, 1998, p. 592-646

8 C.F. Yoloton, F.H. Froes, R.F. Malone, “Alloy element effects in metastable titanium alloys”, Metall. Trans. A, Vol 10A, 1979, p.132-134

9 G. Terlinde, T. Witulski, G. Fischer, “Forging of titanium” in “Titanium and titanium alloys” (ed. M. Peters, C. Leyens), Wiley-Vch-Verlag, Weinheim, 2003, p. 289-304

10 H. Chladil, “Entwicklung und Charakterisierung von hoch Niob-haltigen γ-Titanaluminid Legierungen”, Dissertation, Montanuniversität Leoben, 2007

11 H. W. Rosenberg, “The science, technology and application of titanium” Pergamon Press, Oxford, UK, 1970, p. 851

12 M. Peters., C. Leyens, W.A. Kaysser, “IMI 834 und TIMETAL 1100 – Warmfeste Titanlegierungen für die Luft- und Raumfahrt“, Deutsche Forschungsanstalt für Luft- und Raumfahrt e.V., 1994

13 D.G. Lewicki, W. C. Emmerling, D. Altobelli, S. Seng, C. Frankenberger, L. Fila, „TF41 Engine fan disk seeded fault crack propagation test“, Glenn Research Center, 2004

14 D. Eylon, S. Fujishiro, P. J. Postans, F. H. Froes, “High-temperature titanium alloys – A review” (ed. F. H Froes, D. Eylon, H. B. Bomberger), The titanium development association, p. 87-94

15 S.R. Seagle, G.S. Hall, H.B. Bomberger, “High temperature properties of Ti-6Al-2Sn-4Zr-2Mo-0.009Si”, Metals Engineering Quarterly, February 1975, p. 48-54

16 D. F. Neal, S. P. Fox, “The influence of silicon an silicides on the properties of near-alpha titanium alloys”, Titanium ’92 science technology (ed. F. H. Froes, I. Caplan), The minerals, metals & materials society, 1993, p. 287-294

17 N. Singh, Gouthama, V. Singh, “Low cycle fatigue behaviour of Ti alloy Timetal 834 at 873K”, International Journal of Fatigue (Article in press), 2006

18 M. Peters, Y.T. Lee, K.-J. Grudhoff, H. Schurmann, G. Welsch, “Influence of processing on microstructure and mechanical properties of Ti-1100 and IMI 834” in “Microstructure/Property relationships in titanium aluminides and alloys” (ed. Y.-W. Kim, R. R. Boyer), The Minerals, Metals & Materials Society, 1991, p. 533-548

19 H. Mughrabi, H. Kestler (V), H. Renner, H. J. Maier, M. Baumgartner, K. H. Gradl, “Optimierung der Wärmebehandlung der geschmiedeten Titanlegierung IMI 834 zur Verbesserung der Hochtemperaturfestigkeitseigenschaften” in “Symposium – Neue Werkstoffe in Bayern”, p. 185-204

20 P. Wanjara, M. Jahazi, H. Monajati, S. Yue, “Influence of thermomechanical processing on microstructural evolution in near-α alloy IMI 834”, Materials Science and Engineering A 416, 2006, p. 300-311

21 P. Wanjara, M. Jahazi, H. Monajati, S. Yue, J.-P. Immarigeon, “Hot working behavior of near-α alloy IMI834”, Materials Science and Engineering A 396, 2005, 50-60

22 M. T. Cope, M. J. Hill, The influence of ageing temperature on the mechanical properties of IMI 834”, Rolls-Royce, Sixth world conference on titanium,1988

23 D. Weinem, J. Kumpfert, M. Peters, W. A. Kaysser, „Processing window of the near-α alloy Timetal-1100 to produce a fine grained β-structure, Materials Science and Engineering A 206, 1996, p. 55-62

24 H. Sibum, “Titanium and titanium alloys – From raw material to semi-finished products” in “Titanium and titanium alloys” (ed. M. Peters, C. Leyens), Wile-Vch-Verlag, Weinheim, 2003, p. 231-244

25 F. Ma, W. Lu, J. Quin, D. Zhang, “Microstructure evolution of near-α titanium alloys during thermomechanical processing”, Materials Science and Engineering A 416, 2006, p. 59-65

26 C. Leyens, “Oxidation and protection of titanium alloys and titanium aluminides”, in “Titanium and titanium alloys” (ed. M. Peters, C. Leyens), Wile-CH-Verlag, Weinheim, 2003, p. 187-230
27 K. V. S. Srinadh, V. Singh, “Oxidation behavior of the near α-titanium alloy IMI 834”, Bulletin of Material Science, Vol. 27, No. 4, 2004, p. 347-354
28 C. Leyens, H Gedanitz, “Long-term oxidation of orthorhombic alloy Ti-22Al-25Nb in air between 650℃ and 800℃”, Scripta Materialia , 1999, 41(8), p. 901-906
29 C. Leyens, M. Peters, W. A. Kaysser, “Oxidation behavior of near-α titanium alloys and their protection by coatings”, Titanium ’95: Science and Technology, p. 1935-1942
30 E. Kozeschni, B. Buchmayr, “MatCalc - A simulation tool for multicomponent thermdynamics, diffusion and phase transformation kinetics”, Mathematical Modelling of Weld Phenomena, Vol. 5, Location, 2001, p. 349
31 N. Saunders, A. P. Miodownik, “CALPHAD (Calculation of Phase Diagrams): A Comprehensive Guide”, Pergamon, Cambridge, 1998
32 G. Petzow, “Metallographisches, keramographische, plastographisches Ätzen”, Bornträger, 6. Auflage, Berlin, Stuttgart, 1994
33 R. Allmann, “Röntgenpulverdiffraktometrie: Rechnergestützte Auswertung, Phasenanalyse und Strukturbestimmung” Springer, Berlin Heidelberg, 2003
34 Bruker-AXS, http://www.bruker-axs.de/index.php?id=topas&L=1, Februar 2007
35 D. Brandon, W. D. Kaplan, „Mikrostructural characterization of materials”, Wiley & Sons, 2003
36 C. R. Brundl, C. A. Evans Jr., S. Wilson, „Encyclopedia of materials characterization”, Butterworth-Heinemann, 1992
37 D. B. Williams, C. B. Carter, “Transmission electron microscopy”, Plenum publishing corporation, 1996
38 R. Bürgel, Handbuch der Hochtemperatur-Werkstofftechnik, Vieweg, 1998
39 R. Joos, by private communications, DaimlerChrysler AG, 2007

Appendix

A. Tensile tests

A.1. Tensile test results on LCS material

condition (HT)	*E [GPa]*	*Rm [MPa]*	*Rp0.01 [MPa]*	*Rp0.1 [MPa]*	*Rp0.2 [MPa]*	temperature
as-extruded	116.8	1067.4	776.0	912.3	954.7	RT
650℃ 8h AC	121.1	1097.1	879.0	1021.0	1056.3	RT
850℃ 8h WQ	117.7	1103.9	719.7	914.0	967.0	RT
1010℃ 20min WQ 650℃ 8h AC	122.8	1238.8	1133.0	1204.0	1235.0	RT
as-extruded		314.7			170.1	800℃
650℃ 8h AC		332.3			185.1	800℃
850℃ 8h AC		381.2			221.5	800℃
850℃ 8h WQ		370.5			225.5	800℃
850℃ 8h AC 650℃ 8h AC		365.6			220.6	800℃
850℃ 8h WQ 650℃ 8h AC		372.8			226.9	800℃
1010℃ 20min WQ 650℃ 8h AC		315.5			156.9	800℃
800℃ 8h WQ		344.3			207.1	800℃
800℃ 24h WQ		358.4			226.3	800℃

A.2. Tensile test results on VBS material

condition (HT)	*E [GPa]*	*Rm [MPa]*	*Rp0.01 [MPa]*	*Rp0.1 [MPa]*	*Rp0.2 [MPa]*	temperature
as-extruded	122.1	1336.1	900.7	1072.3	1130.7	RT
650℃ 2h AC	123.9	1420.9	1114.3	1291.0	1329.3	RT
as-extruded		313.9			148.5	800℃
750℃ 2h AC		323.0			158.1	800℃
850℃ 8h WQ		352.5			181.8	800℃

A.3. Tensile test results on VBU material

condition (HT)	*E [GPa]*	*Rm [MPa]*	*Rp0.01 [MPa]*	*Rp0.1 [MPa]*	*Rp0.2 [MPa]*	temperature
850℃ 8h WQ	125.9	1328.4	1022.7	1141.0	1178.0	RT
800℃ 24h WQ		887.7			574.9	600℃
as-extruded		359.2			184.4	800℃
850℃ 8h WQ		358.4			185.8	800℃
800℃ 24h WQ		370.5			195.2	800℃

A.4. Tensile test results on VBT material

condition (HT)	*E [GPa]*	*Rm [MPa]*	*Rp0.01 [MPa]*	*Rp0.1 [MPa]*	*Rp0.2 [MPa]*	temperature
WBH 800℃ 24h WQ	128.3	1354.1	942.3	1176.3	1226.3	RT
as-extruded		321.8			160.6	800℃

B. Dilatometry and deformation tests

Dilatometer Sample 1 (1 mm/s, 1090℃, cooling condi tion 1):

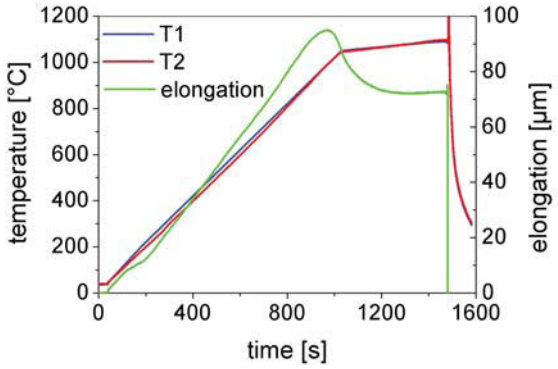

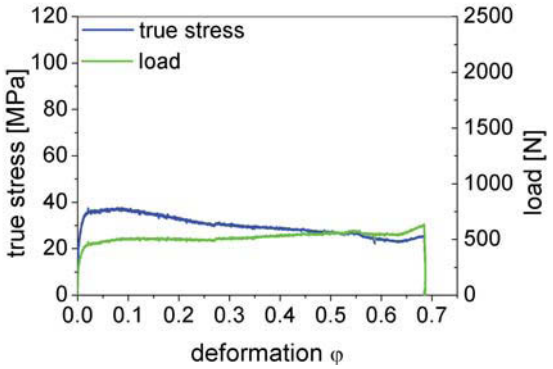

Dilatometer Sample 2 (10 mm/s, 1090℃, cooling cond ition 1):

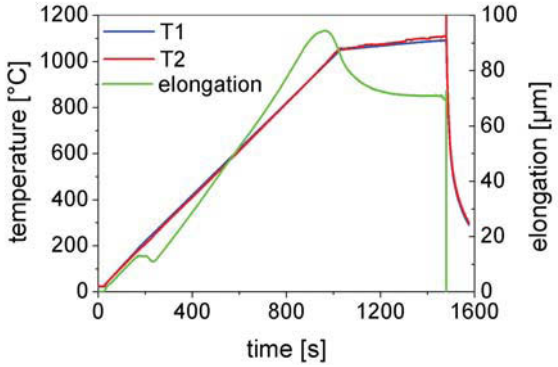

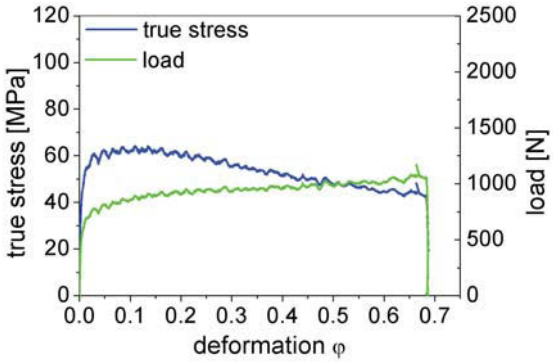

Dilatometer Sample 3 (100 mm/s, 1090℃, cooling con dition 1):

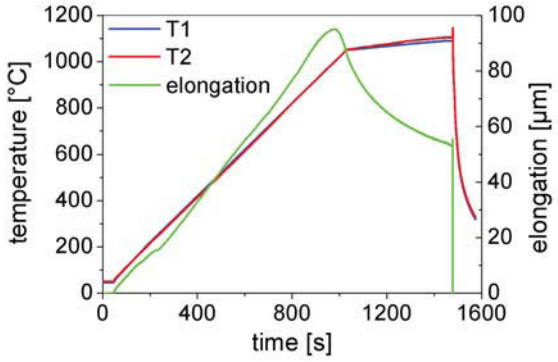

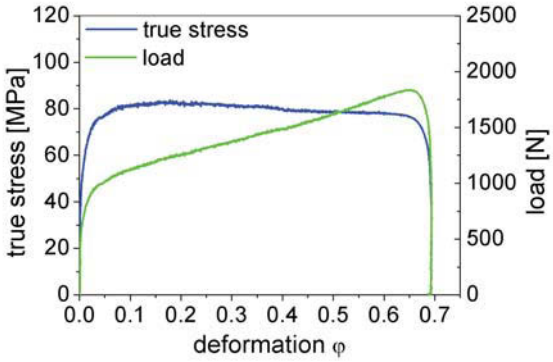

Dilatometer Sample 4 (100 mm/s, 1070℃, cooling con dition 1):

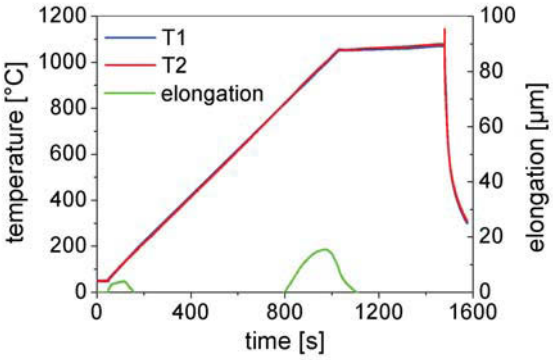

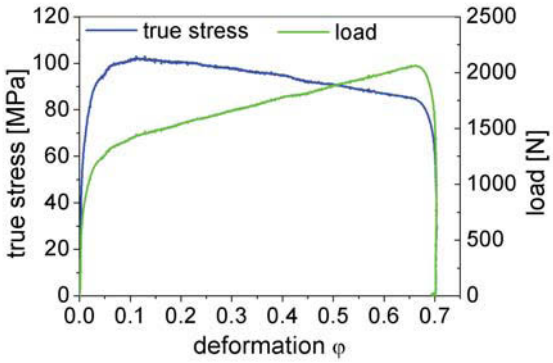

Dilatometer Sample 5 (100 mm/s, 1110℃, cooling con dition 1):

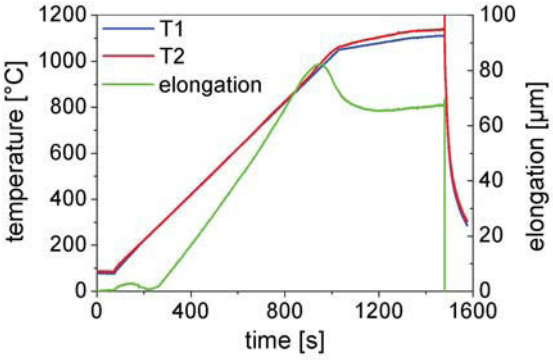

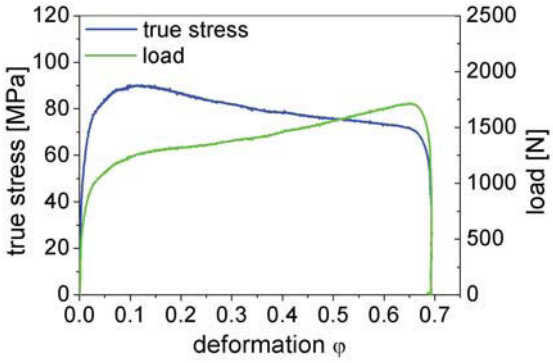

Dilatometer Sample 6 (1 mm/s, 1090℃, cooling condi tion 2):

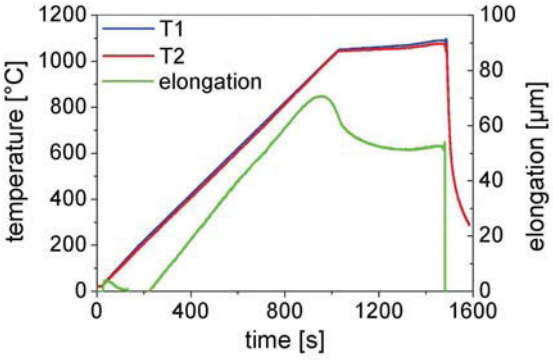

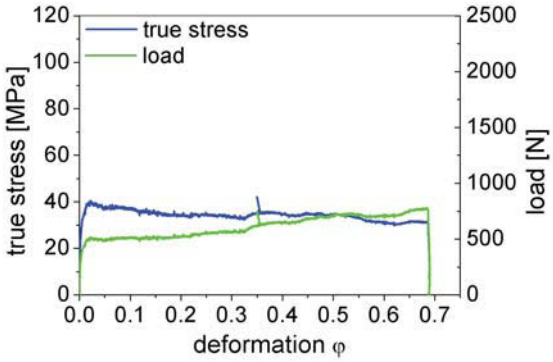

Dilatometer Sample 7 (10 mm/s, 1090℃, cooling cond ition 2):

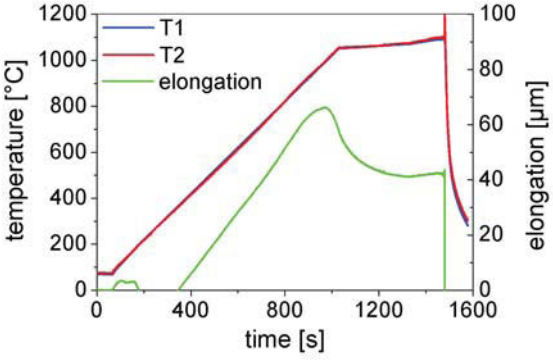

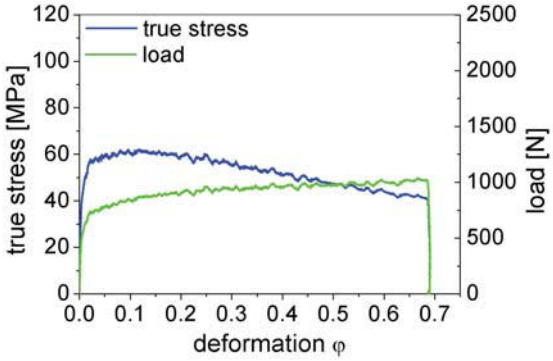

Dilatometer Sample 8 (100 mm/s, 1090℃, cooling con dition 2):

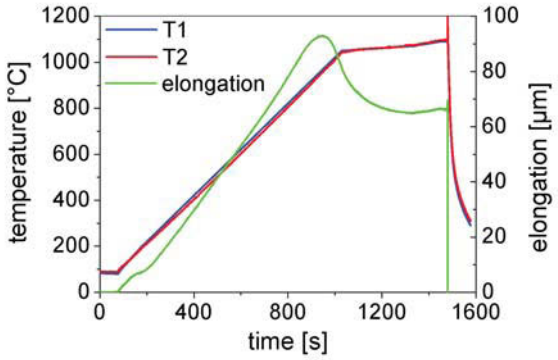

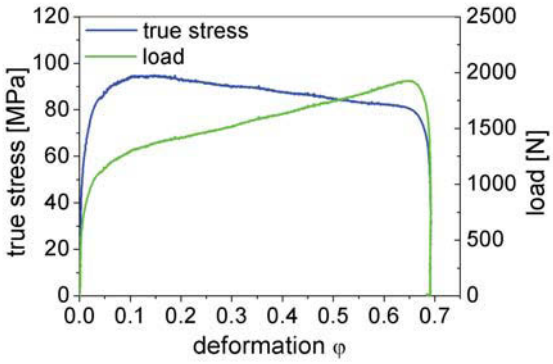

Dilatometer Sample 9 (100 mm/s, 1070℃, cooling con dition 2):

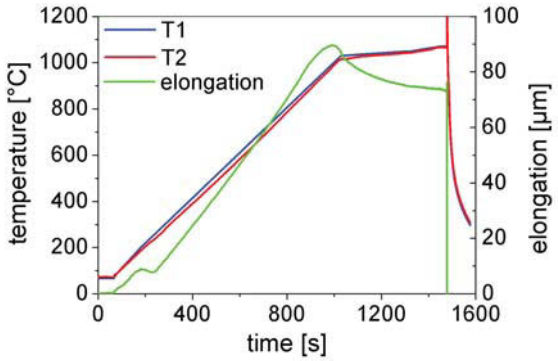

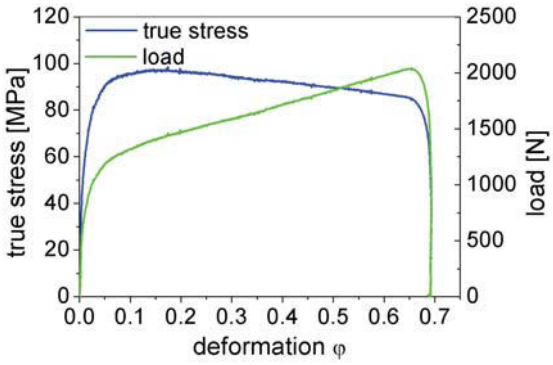

Dilatometer Sample 10 (100 mm/s, 1110℃, cooling co ndition 2):